Research Updates

Magnetic proximity effects in topological insulator heterostructures: Implementation and characterization

A. J. Grutter [1] and Q. L. He[2,3]

[1]*NIST Center for Neutron Research, National Institute of Standards and Technology, Gaithersburg, Maryland 20899, USA*
[2]*International Center for Quantum Materials, Peking University, Haidian District Beijing 100871, China*
[3]*Interdisciplinary Institute of Light-Element Quantum Materials and Research Center for Light-Element Advanced Materials, Peking University, Beijing 100871, China*

In this progress report, we examine recent efforts towards the introduction of magnetic order into topologically nontrivial systems through magnetic proximity effects, with a particular emphasis on the methods of characterizing magnetization induced at the interface. We focus on the challenges associated with comparing magneto-transport measurements with magnetic scattering and spectroscopy techniques, considering the limitations and potential artifacts associated with topological insulator heterostructures. Taking the $(Bi, Sb)_2(Se, Te)_3$ family of three-dimensional topological insulators as an example, we discuss the results associated with a wide range of magnetically ordered reservoirs and highlight the wide discrepancies in reported magnetic proximity effect strengths detected using different characterization techniques. Finally, we discuss the outlook of magnetic proximity effects in topological insulator heterostructures as a route towards a higher-temperature quantum anomalous Hall effect.

I. INTRODUCTION

Topologically nontrivial systems have emerged in the past decade as an exciting new frontier in condensed matter physics research, exhibiting novel quantum effects with the potential to revolutionize quantum computing and next generation spintronics [1–11]. Typical examples such as topological insulators (TIs, e.g., Bi_2Te_3), topological crystalline insulators (e.g., SnTe), Chern insulators [e.g., $Cr_x(Sb, Bi)_{2-x}Te_3$], Weyl semimetals (e.g., TaAs), and Dirac semimetals (e.g., Na_3Bi, Cd_3As_2) host nontrivial topology in their electronic band structures with unconventional linear responses in their bulks and anomalous gapless states at their boundaries [12–19]. The first three are gapped bulk insulators, and can be quantified by topological invariants such as the Z_2 invariant, with a value of either 0 or 1, or a Chern number, with a value of either 0 or ± 1, ± 2, etc. [1,2]. In contrast, the last two are gapless semimetals with crossings between the conduction band and valence band, which can be characterized by the number and type of these band crossings [8–11]. The value of the topological invariant, which depends on the dimensionality and the symmetries of the system, consequently allows the classification of topologically trivial and nontrivial systems. In this progress report, we focus on the insulator systems whose topologies depend on the wave functions of their valence bands in the entire Brillouin zone.

Among the foremost goals of research into topological matters is the extension of novel quantum phenomena such as the quantum anomalous Hall (QAH) state to more accessible, technologically relevant temperature regimes. This state originates in the gap opened in the surface states of a TI through time reversal symmetry breaking, which allows the manifestation of dissipationless chiral edge currents and an insulating bulk [20–22]. A quantum system that can accommodate such a state is thus referred to as a QAH insulator or Chern insulator since the edge state can be characterized by the Chern number. A QAH insulator can be realized in a TI in which time-reversal symmetry is broken by perpendicular long-range magnetic order, which may be introduced through three schemes:

Scheme I: The introduction of magnetic dopants, such as Cr or V, into a TI, e.g., $(Bi, Sb)_2Te_3$ [22–25].

Scheme II: The magnetic proximity effect (MPE), in which a net magnetization is induced by interfacing a TI (most commonly a thin film) with a reservoir of magnetic order with perpendicular magnetic anisotropy (most commonly a thin film but sometimes a cleaved single crystal) [26–49].

Scheme III: Fabrication of a stoichiometric TI with an intrinsic magnetic order, e.g., $MnBi_2Te_4$ [50–52].

While stabilization of the QAH effect primarily requires the breaking of time-reversal symmetry, which in principle can be readily fulfilled by the development of perpendicular ferromagnetic order, the magnetic ordering temperatures are surprisingly at least one order of magnitude higher than the temperature at which the QAH effect is observed. For example, magnetically doped TIs supporting the QAH effect generally exhibit Curie temperatures (T_Cs) between 10 K and 30 K, but the QAH effect in such systems remains limited to temperatures below 2 K. This low temperature limit greatly hinders the further development and application of QAH insulators.

More specifically, the highest QAH temperatures so far realized through the aforementioned three schemes of doping, proximity, and intrinsic magnetic order are 2 K, 0.1 K, and 1.9 K, respectively; none of which exceed even liquid helium temperatures [48,53,54]. While the factors hindering realization of the QAH effect at higher temperature are not yet fully understood, the reduced temperature is most commonly attributed to two mechanisms.

(1) Spatially inhomogeneous distribution of the exchange gap: The exchange gap has been reported to be in the range of 30 meV–50 meV, in principle large enough to enable manifestation of the QAH effect at high temperature [55,56]. However, the random distribution of the magnetic dopants that couple to the surface Dirac electrons can result in a spatial fluctuation of the magnitude of the exchange gap [57]. Such a fluctuation may shrink the overall effective exchange gap and require a lower temperature to overcome thermal fluctuations. On the other hand, precise, uniform control of atomic-site substitution of the magnetic dopant remains a challenge. A recent first-principles calculation points out that the formation energy of the magnetic dopant (e.g., Cr) leads to preferential substitution on the Bi site rather than Sb, which implies a complex set of competing mechanisms influencing the inhomogeneity of the exchange gap in the QAH insulator $Cr_x(Bi, Sb)_{2-x}Te_3$ [58].

(2) Trivial transport paths in the bulk arising from defects and impurities: Scanning tunneling microscopy studies have observed Bi_{Te} or Sb_{Te} antisites, Sb/Bi vacancies within the TI matrix, and magnetic dopant antisites (Cr_{Te}, Cr_{Bi}, or Cr_{Sb}) [56,59–61]. An excess of such imperfections introduces chemical disorder in TIs which then deviates from the ideal chemical composition and crystalline structure. This may occur at concentrations such that they overwhelm the defect tolerance of the topological protection and lead to the formation of parasitic conduction channels in the bulk of the TI [53]. Alternatively, additional states or bands will form near the Fermi level within the exchange gap due to these defects and impurities, which will also reduce the magnitude of the effective exchange gap [60].

The two mechanisms discussed above commonly occur in the doped TIs of Scheme I, although modulation doping geometries have already been shown to significantly improved the situation [53,62]. With a sufficiently uniform high-quality interface, TIs of Scheme II may in principle largely avoid the challenges associated with inhomogeneity but so far a satisfying magnet for proximity remains elusive. Although the QAH effect has been achieved by interfacing $(Bi, Sb)_2Te_3$ with Cr-doped ZnTe, the Cr dopants in ZnTe also introduce inhomogeneity [48]. Hence, the temperature to realize the QAH effect by MPE in this heterostructure remains as low as 0.1 K, much lower than the Curie temperature of Cr-doped ZnTe (60 K). It is believed that TIs of Scheme III should avoid all of these problems. However, similar antisite defects associated with metal substitutions of Te (e.g., Bi_{Te}/Mn_{Te}) and intermixing between the metals (i.e., Bi_{Mn} and Mn_{Bi}) are observed extensively in $MnBi_2Te_4$, which similarly results in spatial fluctuations in the local density of states and the exchange gap near the Fermi level [63,64]. Consequently, even when examining a nominally stoichiometric TI with intrinsic magnetic order, the manifestation temperature of the QAH

effect remains much lower than the Néel temperature of the TI (25 K). In short, it seems that the above two mechanisms cannot currently be fully addressed by either Scheme I, i.e., the magnetically doped TI, or Scheme III, i.e., the stoichiometric TI.

There is therefore considerable interest in stabilizing a high-temperature magnetic phase in TIs through Scheme II, the MPE, in which a magnetization is induced/enhanced across the interface of a heterostructure between a magnetically ordered material and a layer without/with magnetic order. Highly insulating magnetically ordered layers are strongly preferred in order to avoid the complexities associated with current being shunted around the TI layer. A high Curie or Néel temperature is also desirable in the ordered layer, in order to avoid limiting the ordering temperature of the adjacent TI layer being magnetized. Critically, a sufficiently high-quality interface may allow the introduction of a net magnetization in the TI without additional defects, preserving the topological surface states which are of principal interest. An appropriate substrate or buffer layer with a high Curie temperature and matched lattice to TIs could minimize imperfections from the mismatch. It would be ideal to combine either the doping or intrinsic order schemes with Scheme II to achieve a QAH state such that both the magnitude and spatial uniformity of the exchange gap can be improved through the assistance of an MPE.

However, despite intensive effort towards the stabilization of MPEs through interfacing topological matter with magnetically ordered reservoirs, a high-temperature QAH state remains elusive. Indeed, as noted above, the sole example of proximity-induced QAH effect is limited to temperatures of 0.1 K or below and suffers from the same inhomogeneity as doped and stoichiometric systems [48]. Further, the literature is extremely disparate and inconsistent, perhaps owing to the difficulty of unambiguously identifying the presence of an MPE, let alone understanding the influence of interfacial defects or uniformity across the interface. Of particular note is the disagreement between different techniques, where scattering and spectroscopic approaches often yield results which are at odds with transport or bulk magnetometry.

For clear progress to be made in enhancing the strength and uniformity of the exchange gap induced by magnetic proximity, the limitations and advantages of various characterization techniques must be clearly understood in the context of proximity-magnetized TI systems. In this progress report, we examine the most commonly applied characterization techniques used to probe proximity magnetized TI heterostructures, with a particular focus on the most-explored $(Bi, Sb)_2(Se, Te)_3$ family as a model system. In Sec. II we discuss the application of magnetometry, transport, neutron, and x-ray scattering, and magnetic x-ray spectroscopy techniques to the problem at hand. While these are the most commonly applied approaches, other probes such as second harmonic generation, muon spin rotation spectroscopy, or point-contact Adreev reflectivity are increasingly being applied. These techniques will be discussed in the context of individual systems in Sec. III, where we examine in detail the progress made in applying a wide range of magnetic reservoirs to the $(Bi, Sb)_2(Se, Te)_3$ family.

Throughout the following discussion, we will generally make the distinction between static and nonequilibrium MPEs, reflecting the growing concern within the field that the act of performing measurements meant to characterize MPEs may in fact induce them during the measurement. This topic will be discussed in much greater detail in the transport characterization section below, but generally may be understood in terms of an inverse spin-Hall or nonlocal anomalous Hall effect leading to magnetoresistance in the presence of current [65–70]. Generally, when we refer to an MPE without further qualification, we refer to a static MPE present in the absence of applied charge current.

This choice of focus and terminology does not by any means indicate a lack of interest in nonequilibrium proximity effects in TI heterostructures. Indeed, there is currently an enormous research effort focused on harnessing current-induced magnetic coupling effects across TI/magnet interfaces for low-power spintronic devices. The large spin-orbit coupling inherent in systems such as $(Bi, Sb)_2Te_3$ provides an exciting avenue for realizing magnetization switching through the associated giant spin-orbit or spin-transfer torques [31,71–78]. For the ultimate implementation of spin-orbit based logic devices incorporating TI layers, a detailed understanding of coupling across the interface will be just as critical as it is in the effort to raise the QAH temperature. Thus, while this research update focuses primarily on static proximity effects and their implications for the QAH effect, many of the topics discussed are relevant for TI-based spintronic devices operating in a nonequilibrium mode.

II. INTERFACE CHARACTERIZATION AND CHALLENGES

A. Magnetometry

Direct characterization of MPEs using magnetometry has long posed particular challenges, as the magnitude of the induced interfacial magnetization is typically significantly smaller than and difficult to separate from that of the magnetically ordered layer. Quantitative bulk techniques such as superconducting quantum interference device (SQUID) magnetometry and vibrating sample magnetometry (VSM) rely on induced voltages as a sample position is swept relative to a SQUID loop or VSM pickup coils, and probe the total magnetic moment present in the sample volume [79–81]. These techniques cannot distinguish between contributions from the magnetically ordered or nonmagnetic layers, so that studies using these techniques generally rely on precise volume normalization and reference standards.

Still, a 2020 comparison between VSM and x-ray resonant magnetic reflectivity (XRMR) by Moskaltsova *et al.* suggested that the strong MPE expected in Pt interfaced with a ferromagnetic metal can exceed the VSM detection threshold [82]. While MPEs in TI-based heterostructures are expected (and typically reported) to be significantly weaker than those in Pt, bulk magnetometry may still provide insight in cases where the net magnetization of the magnetically ordered reservoir is small enough that the proximity-magnetized layer represents a significant fraction of the total net moment in the system. Although such situations may be challenging to
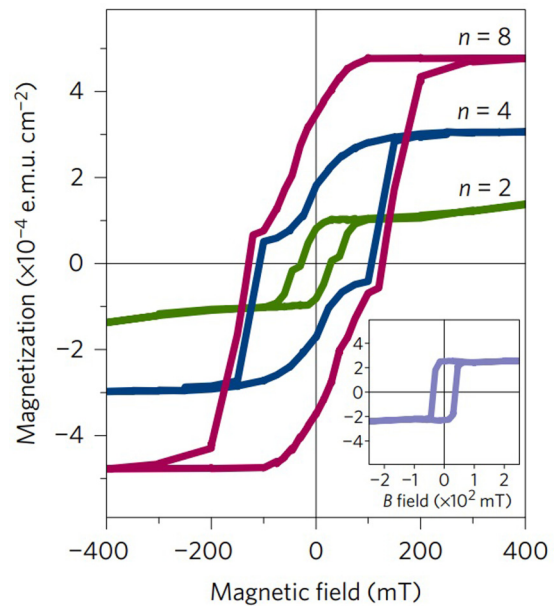

FIG. 1. Magnetization vs applied field of a series of Cr-doped $(Bi, Sb)_2Te_3/CrSb$ superlattices with increasing number of superlattice period repeats, collected using SQUID magnetometry. (Inset) Measurement of a control sample of a Cr-doped $(Bi, Sb)_2Te_3$/Undoped $(Bi, Sb)_2Te_3$. Use of an antiferromagnet magnetic reservoir results in the magnetic TI dominating the magnetization. Adapted from Q. L. He *et al.*, Nature Materials **16**, 94 (2017) [35]. 1 emu/cm^2 = 10 A.

realize due to reported threshold effects and linear scaling of the MPE magnitude with the total proximity reservoir magnetization in metal-metal systems, the local orbital overlap polarization mechanism of MPEs may offer a route around these limitations [83,84]. Specifically, compensated ferrimagnets such as the rare earth garnets or antiferromagnets with spin-polarized planes at the interface may yield localized MPEs while contributing negligibly to the net magnetization, as exemplified by the Cr-doped $(Bi, Sb)_2Te_3/CrSb$ system shown in Fig. 1 [35,85]. In such cases, SQUID magnetometry has been shown to provide useful information on the MPE [35,36]. Still, many examples of suspected MPEs are expected to yield signals below the noise floor of all but the most sensitive modern magnetometry tools.

Magneto-optic Kerr effect (MOKE) magnetometry is an optical magnetometry technique which is becoming more widely used in the characterization of MPEs, especially in layered two-dimensional Van der Walls systems [86–88]. MOKE magnetometry relies on optical methods of resolving the change in polarization direction (the Kerr rotation) of polarized light reflected from a magnetic material, often a thin film [86]. Although less quantitative that either SQUID or VSM magnetometry, the variance in the optical responses of different materials allow a greater degree of separation between the magnetizations of different layers. For example, in a heterostructure where the magnetically ordered layer induces an extremely small Kerr rotation, the majority of the MOKE signal may actually originate in the proximitized layer. In fact, several studies have made use of the limited Kerr signal originating in $Y_3Fe_5O_{12}$ to directly identify the
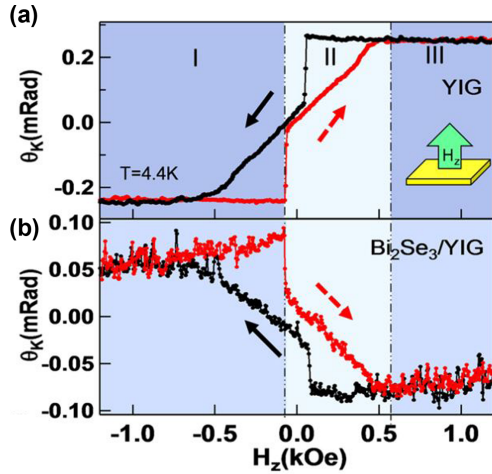
FIG. 2. (a) Applied magnetic field-dependent Kerr rotation associated with (a) a bare $Y_3Fe_5O_{12}$ film and (b) 8 nm of Bi_2Se_3 grown on a $Y_3Fe_5O_{12}$ film. A change in the sign of the Kerr rotation is observed. Adapted with permission from M. Lang *et al.*, Nano Lett. **14**, 6, 3459 (2014) [89]. Copyright 2014 American Chemical Society. 1 Oe = 79.6 A/m.

induced magnetization in an adjacent TI layer [30]. Alternatively, in the case of antiparallel coupling shown in Fig. 2, the two layers may yield opposite sign Kerr effects due to the relative surface sensitive of a MOKE probe, so that a sign change is evident upon growth of a proximitized overlayer [89]. Lastly, the depth sensitivity of MOKE, which uses light that penetrates approximately 20 nm into a metal film, may allow separation of different layer contributions through careful thickness studies [86]. Even in cases where the MOKE signal is extremely small or primarily originates in the magnetically ordered layer, high-precision and temperature-dependent measurements can allow the contribution of an MPE to be isolated [90,91]. Thus, while much caution must be taken in the interpretation of magnetometry-based efforts to probe MPEs, valuable information may be obtained through the careful application of these techniques.

B. Transport and quantization

Magneto-electric transport measurements are among the most powerful and widely-employed tools when searching for signs of an MPE. The most commonly cited indicators of magnetic coupling or an MPE take the form of weak antilocalization suppression or the emergence of an anomalous Hall effect. In TIs, the π Berry phase of the surface states is affected by spin-dependent interactions, e.g., magnetic exchange coupling with either magnetic impurities or a magnetic layer in adjacent to the TI surface. Therefore, in many cases, the suppression of weak antilocalization has been implicated as evidence of a gap opening in the TI. However, this suppression can be induced by magnetic perturbations to the surface states with random magnetization direction rather than uniform long-range magnetic order. This may result in two outcomes: either random spatial distribution of the local gap across the TI, which may not form an effective gap overall, or magnetic scattering caused by these randomly distributed
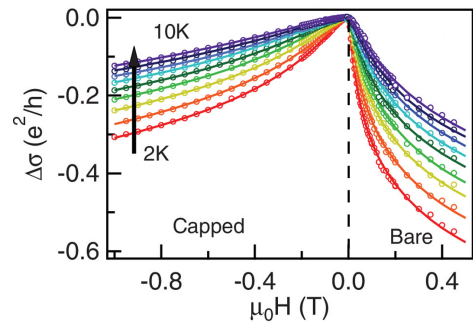

FIG. 3. Temperature-dependent magnetoconductance vs applied magnetic field for Bi_2Se_3 (Bare) and Bi_2Se_3/GdN (Capped) films, showing weak antilocalization suppression in the capped sample. Reproduced from A. Kandala *et al.*, Appl. Phys. Lett. **103**, 202409 (2013) [49], with the permission of AIP Publishing.

magnetic perturbations, which reduces the phase coherence length of the surface carriers and suppresses weak antilocalization [49,92–94]. This second case is well illustrated by Fig. 3, which shows a report of weak antilocalization suppression in the Bi_2Se_3/GdN system which was not attributed to opening a gap in the surface states. As a result of this ambiguity, Hall measurements have come to be more commonly cited as direct transport evidence of a net magnetization in the TI layer associated with opening a gap in the surface states.

In typical Hall measurements, the Hall resistivity of a ferromagnet in a weak applied magnetic field H_z is characterized by the semiempirical relation $\rho_{xy} = \rho_{xy}^0 + \rho_{xy}^A = R_H H_z + 4\pi R_s M_z$, where R_H and R_s are normal and anomalous Hall coefficients, respectively. The ordinary Hall resistivity (ρ_{xy}^0) is linearly proportional to H_z through R_H, which is simply related to the carrier concentration in a single-band system. On the other hand, the anomalous Hall resistivity ρ_{xy}^A is proportional to the spontaneous magnetization M_z as well as R_s, which involves both extrinsic and intrinsic mechanisms. The simultaneous observation of both ρ_{xy}^0 and ρ_{xy}^A in TI MPE heterostructures is illustrated in Fig. 4.

The main extrinsic scattering contributions originate in the skew and side-jump mechanisms, both of which originate in impurity or disorder scattering. Therefore, in a simple heterostructure consisting of a nonmagnetic conductor and a magnetic insulator, the ρ_{xy}^A obtained from
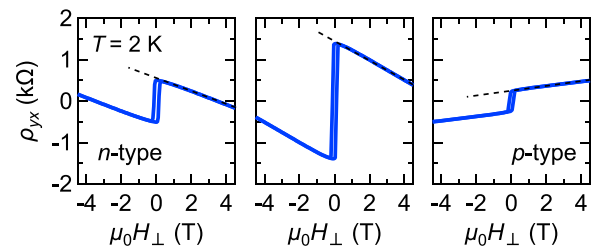

FIG. 4. ρ_{xy} vs applied magnetic field for a series of $Cr_2Ge_2Te_6$/(Bi, Sb)$_2$Te$_3$/Bi$_2$Te$_3$/(Bi, Sb)$_2$Te$_3$/Cr$_2$Ge$_2$Te$_6$ sandwich heterostructures with varying Bi, Sb ratios. Both the linear normal Hall effect and AHE may be clearly observed, with the normal Hall effect changing sign as the Bi/Sb ratio is varied, changing the (Bi, Sb)$_2$Te$_3$ from n-type to p-type. From M. Mogi *et al.* (2019) [47].

TABLE I. Typical R_{xy} values and magnetic transition temperatures reported in a range of TI-based MPE heterostructures.

Proximity reservoir	Topological system	Approximate R_{xy}	T_C	Reference
$Tm_3Fe_5O_{12}$	$(Bi_xSb_{1-x})_2Te_3$	10^{-1} Ω at 300 K	$\geqslant$300 K	[26]
$Y_3Fe_5O_{12}$	$(Bi_xSb_{1-x})_2Te_3$	10^{-1} Ω at 13 K	$\leqslant$100 K	[27]
$Y_3Fe_5O_{12}$	$Bi_{1.89}Cr_{0.11}Se_3$	10 Ω at 5 K	$\geqslant$13 K	[28]
$Y_3Fe_5O_{12}$	$(Bi_{0.16}Sb_{0.84})_2Te_3$	10^0 Ω at 1.9 K	$\approx$50 K	[29]
$Y_3Fe_5O_{12}$	Transferred Bi_2Se_3	10^0 Ω at 1.9 K	$\approx$30 K	[30]
$BaFe_{12}O_{19}$	Bi_2Se_3	10^{-2} Ω at 3 K	N/A	[31,32]
$LaCoO_3$	Bi_2Se_3	10^{-1} Ω at 1.7 K	>85 K	[33,34]
Fe_3O_4	Bi_2Te_3	10^0 Ω at 2K	>85 K	[94]
CrSb	$Cr:(Bi, Sb)_2Te_3$	10^2 Ω at 1.9 K	90 K	[35]
CrSb	$(Bi, Sb)_2Te_3$	10^4 Ω at 1.9 K	90 K	[36]
$Ga_{1-x}Mn_xAs$	$(Bi, Sb)_2(Te, Se)_3$	10^2 Ω at 0.1 K	1 K	[37]
EuS	Bi_2Se_3	10^{-1} Ω at 5 K	17 K	[38–40]
$Dy:Bi_2Te_3$	$Cr:Sb_2Te_3$	10^0 Ω at 1.8 K	140 K	[97]
CrSe	$(Bi, Sb)_2Te_3$	10^2 Ω at 2 K	120 K	[41]
MnTe	$(Bi, Sb)_2Te_3$	10^0 Ω at 1.9 K	12 K	[42]
Cr_2O_3	$Sb_{1.8}Cr_{0.2}Te_3$	500 Ω at 2 K	40 K	[43]
Cr_2O_3	$Cr:(Bi, Sb)_2Te_3$	$\frac{h}{e^2}$ Ω at 1.9 K	30 K	[44]
$Cr_2Ge_2Te_6$	Bi_2Te_3	10^{-1} Ω at 2.5 K	110 K	[45]
$CrGeTe_3$	$(Bi_xSb_{1-x})_2Te_3$	10^2 Ω at 6.6 K	70 K	[46]
$Cr_2Ge_2Te_6$	$(Bi, Sb)_2Te_3$	$>10^3$ Ω at 2.5 K	100 K	[47]
$Zn_{1-x}Cr_xTe$	$(Bi_ySb_{1-y})_2Te_3$	$\frac{h}{e^2}$ at 30 mK	50 K	[48]

transport measurements is often used to characterize the MPE-induced magnetization of the nonmagnetic conductor. In this case, the magnitude of ρ_{xy}^A can therefore characterize the strength of the MPE. Note that the nonmagnetic conductor here presumably is topologically trivial, and the intrinsic ρ_{xy}^A due to its electronic structure is negligibly small [95].

On the other hand, ρ_{xy}^A of a heterostructure in which the nonmagnetic conductor is replaced by a topological material such as a TI, is mainly determined by intrinsic mechanisms, i.e., the nontrivial Berry curvature of the ground-state wave functions over the whole Brillouin zone. The magnitude such a of ρ_{xy}^A is in this case independent of material parameters such as the impurity and disorder densities as long as they are within the tolerance of the topological protection. Thus, the carrier mobility as an indicator of scattering is again not crucial due to the topological protection, as exemplified by a QAH insulator made from a magnetically doped TI [96]. Due to the topological nature of the Berry curvature, ρ_{xy} will instead be quantized to some universal constant. In the case of a TI/magnetic insulator heterostructure with an interfacial MPE, Dirac electrons couple with the induced magnetization via an exchange interaction, which breaks the time reversal symmetry and opens an exchange gap in the Dirac surface states. Ideally, as long as the Fermi energy is within this exchange gap, the Hall resistance will be quantized to $\frac{h}{e^2} \approx$ 25.8 kΩ (where h is the Planck's constant and e is the charge of an electron), which a key signature of the QAH effect. This effect is independent of the magnitude of the magnetization of the TI as long as this magnetization is perpendicular to the basal plane and can fully gap out the Dirac surface states. However, in most experimental results so far, the obtained ρ_{xy} (or the Hall resistance R_{xy}) values for various TIs interfacing with normal magnetic insulators/semiconductors are much

smaller than this quantized value. Table I summarizes these transport results (including R_{xy} and T_C).

As can been seen in Table I, magnetic oxides and nitrides are popular systems which are convenient for probing the induced ρ_{xy}^A in an adjacent TI due to their strong magnetic order and highly insulating nature in transport experiments. In barium hexaferrite ($BaFe_{12}O_{19}$), rhombohedral perovskite $LaCoO_3$ or the rare-earth garnets $Tm_3Fe_5O_{12}$ and $Y_3Fe_5O_{12}$, T_C of the induced ferromagnetic order, as determined from ρ_{xy}^A, is usually greater than 100 K. However, the resulting R_{xy} is relatively small, ranging from 10^{-1} Ω to 10^1 Ω at low temperature [26–28,30–34]. GdN, on the other hand, shows no clear MPE-related anomalous Hall effect induced in the adjacent TI [49]. Cr_2O_3, also seems not to induce any ρ_{xy}^A, but when a magnetically doped TI is interfaced with Cr_2O_3, enhancements of both T_C and R_{xy} were observed [43,44].

In the case of group V compounds, such as the half metal CrSb or the magnetic semiconductor $Ga_{1-x}Mn_xAs$, both of which exhibit high Curie temperatures, Hall resistances from 1 K to 90 K show the observation of a stronger anomalous Hall effect [35,37]. The resulting R_{xy} are much greater than those obtained in garnets, being on the order of 10^2 Ω to 10^3 Ω at low temperature.

For group VI compounds, such as EuS, CrSe, $Cr_2Ge_2Te_6$, MnTe, and $Zn_{1-x}Cr_xTe$, with magnetic ordering temperatures ranging from 17 K to room temperature, most cases of induced magnetic order in TIs show T_C below 100 K, while the resulting R_{xy} range from 10^{-1} Ω to 10^3 Ω [38–40,45–47]. Critically, in a trilayer of $Zn_{1-x}Cr_xTe/(Bi_ySb_{1-y})_2Te_3/Zn_{1-x}Cr_xTe$, the QAH effect was observed at 100 mK, as evidenced by the quantized $R_{xy} \approx$ 25.8 kΩ and vanishingly small magneto-resistance [48]. This is so far the only structure in which the QAH effect has been realized through an MPE.

Several possible reasons may account for the observation of small ρ_{xy}^A in most systems:

(1) The small magnitude of the exchange gap opened by the induced magnetization on the TI surface.

(2) Transport contributions from bulk carriers, which may depend significantly on the relative position of Fermi energy to the exchange gap in the TI.

(3) Transport contributions from additional states within the exchange gap due to impurities and defects.

(4) An inhomogeneous effective exchange gap opened by the magnetic insulator, which may yield Fermi level crossings with the bulk bands.

It must further be mentioned that, in addition to the extrinsic and intrinsic mechanisms discussed above, a nonzero ρ_{xy}^A may be induced by a number of other effects. These include the combined contribution of the spin Hall effect (SHE) and inverse SHE originating in the relativistic spin-orbit coupling of the heterostructure i.e. the so-called "double spin Hall effect" which yields a spin-Hall magnetoresistance [65–68]. Other proposed mechanisms include nonequilibrium proximity effects, present only during transport measurements, or a nonlocal anomalous Hall effect [65,69]. The ρ_{xy}^A from an MPE generally emerges at some onset temperature T_{MPE} which depends on the relative strength of the orbital hybridization and thermal fluctuations. Below T_{MPE}, there is a static spontaneous magnetization induced by the magnetically ordered layer. While the MPE generally contributes to the magnetotransport below T_{MPE}, the ρ_{xy}^A associated with the SHE may manifest at all temperatures below the T_C of the adjacent magnetic material. This SHE contribution thus dominates at elevated temperatures but may not represent a static MPE. Here we note that many magnetic insulator studies in TI MPE heterostructures have high magnetic ordering temperatures (usually above room temperature), below which the spin texture well develops and gives rise to SHE. Interestingly, the sign of ρ_{xy}^A from MPE and SHE, which is materials-dependent, may be different in some cases. A local extremum of ρ_{xy}^A may be observed during cooling if the MPE-induced ρ_{xy}^A at low temperature has an opposite sign to the SHE-induced ρ_{xy}^A at elevated temperature, allowing T_{MPE} to be precisely identified.

Additional complications may occur for heterostructures incorporating a ferrimagnetic insulator as the magnetic reservoir, as two antiparallel spin sublattices and different magnetizations which must now be considered. Some such systems exhibit a critical temperature, T_M, defining the temperature at which the magnetizations of the two sublattices compensate completely. However, the interfacial exchange coupling in the TI layer may follow one spin sublattice at the interface rather than the polarization direction of the net magnetization. Since the MPE is directly related to the orbital overlap across the interface while the spin-Hall effect is related to spin-orbit coupling, the two effects may be dominated by different atomic species and follow different sublattices. Therefore, a sign-change in ρ_{xy}^A across T_M may provide additional information into the roles played by individual sublattices and the SHE [68].

Yet another factor which may result in an apparent nonlinear ρ_{xy} not associated with an MPE is the coexistence
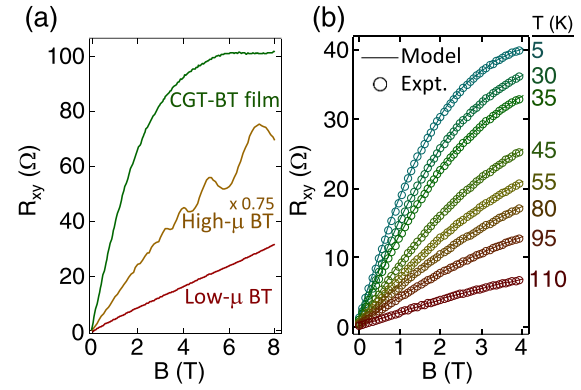

FIG. 5. (a) R_{xy} vs applied magnetic field for low-mobility Bi_2Te_3, high-mobility Bi_2Te_3, and a $Cr_2Ge_2Te_6/Bi_2Te_3$ bilayer at 4.2 K. (b) R_{xy} vs applied magnetic field as a function of temperature for a $Cr_2Ge_2Te_6/Bi_2Te_3$ bilayer. Data have been fitted using a two-band model. Reproduced from L. D. Alegria *et al.*, Appl. Phys. Lett. **105**, 053512 (2014) [45], with the permission of AIP Publishing.

of multiple conduction channels which have similar overall resistivity but dramatically different carrier densities and mobilities. While the above discussion of the ordinary Hall effect assumed a linear response associated with a single dominant carrier, parallel channels such as bulk and interface conduction may occur. The Hall effect from a multicarrier anomalous Hall signal typically yields nonlinear features reminiscent of saturation at high fields of several Tesla but result in little to no apparent hysteresis. Such features are well attested in the literature on TI systems [98–100]. Interestingly, in some systems where magnetic coupling is suspected across a TI/magnetic insulator interface, it is possible to observe multiple contributions to the ρ_{xy}. In the case of a low-coercivity magnetic reservoir, sharp low-field switching in ρ_{xy}^A may then accompany a gradually saturating ρ_{xy}^A feature at higher fields. Here we note the work of Alegria *et al.* on $Cr_2Ge_2Te_6/Bi_2Te_3$, where a high-field nonlinearity (Fig. 5) is observed consistent with either a MPE or multiband transport [45]. In this work, it is noted that the magnetic field nonlinearity occurs at fields far above the $Cr_2Ge_2Te_6$ saturation field, while a low-field hysteresis is also separately observed, indicating that *both* MPE and multi-band carrier effects may be simultaneously present in some systems [45].

C. Neutron scattering

Polarized neutron reflectometry offers a relatively direct route towards the detection of interfacial magnetization induced through MPEs. In PNR measurements, a spin-polarized beam of neutrons is incident on the sample, usually a thin film or multilayer structure, at a relatively shallow angle to the sample surface [101–103]. Measurements are performed in a variable in-plane applied magnetic field, and the reflected neutron intensity is collected as a function of the scattering vector Q along the film normal direction for each polarization cross section of interest. Here we will refer primarily to the nonspin flip reflectivities $R^{\uparrow\uparrow}$ and $R^{\downarrow\downarrow}$, for which both the incident and scattered neutron beams are polarized parallel or antiparallel to the applied magnetic field, respectively. For

these cross sections, the reflected intensity is a function of the depth profile of the nuclear and magnetic scattering length densities (SLDs), determined respectively by the nuclear composition and density or the net in-plane magnetization along the applied magnetic field. Fitting the PNR data therefore allows a depth resolved picture of the structure and magnetism within the sample to be constructed [104,105].

In particular it should be noted that while the majority of topologically nontrivial systems probed using PNR possess strong perpendicular anisotropy, PNR is sensitive only to the net in-plane component of the magnetization [101–104]. Measurements are therefore generally performed in a strong in-plane applied magnetic field in order to align the magnetization of the heterostructures into an orientation where they may be probed by PNR. Most experiments therefore focus on the non-spin-flip scattering, which probes the net in-plane magnetization parallel to the applied field direction, rather than spin-flip scattering, which probes the net in-plane magnetization perpendicular to the applied field. Since the net magnetization is forced to align in-plane with a large magnetic field, it is generally assumed that there are no in-plane moments perpendicular to the applied field, so that the spin-flip reflectivity is vanishingly small.

While PNR has been widely used as a probe of MPEs across a wide range of materials platforms, the analysis may be complicated by a number of factors, some of which are unique to highly layered structures such as $MnBi_2Te_4$ or the prominent $(Bi, Sb)_2(Se, Te)_3$ family of TIs. Firstly, unlike x-ray reflectivity or x-ray scattering, which are able to utilize relatively small spot sizes, PNR beamlines operate with beam sizes which vastly exceed the cross sectional area of samples which may be readily and uniformly fabricated from topologically nontrivial materials. Thus, the entire sample, generally with a cross-sectional area of at least 10×10 mm^2 is probed at once. This means that both roughness contributions from intermixing between layers as well as both short- and long-range thickness variations contribute to the observed interfacial roughness. It is well known that some films of layered $(Bi, Sb)_2(Se, Te)_3$ tend to grow with a terraced surface morphology, manifesting as a series of steps approximately 1 nm high forming islands of varying height on the surface of the film, as illustrated by a series of atomic force microscopy images in the literature [106,107]. Such a large local thickness variation will appear to PNR as an extremely rough, smeared out interface. In contrast, high-resolution scanning transmission electron microscopy performed in the cross-sectional geometry but extending over a much more limited lateral range will show an extremely flat, sharp interface with limited intermixing. These two pictures are not inconsistent, but must be accounted for in the fitting of PNR data.

An additional factor which impacts the analysis of PNR data on topologically nontrivial heterostructures is the fact that the TI layer generally has a relatively low nuclear scattering length density relative to the other layers of the heterostructure. This is due the incorporation of larger elements such as Te, Sb, and Bi which lead to lower atomic number densities in these systems. While in x-ray reflectometry the SLD scales with the atomic number (Z), PNR nuclear SLD is determined by strong force interactions and lacks such compensating
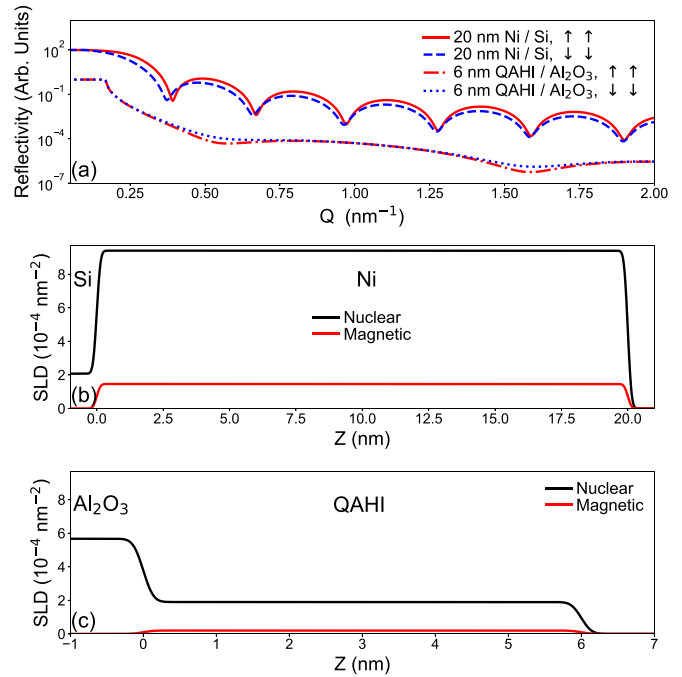

FIG. 6. (a) Simulated PNR signal expected from a 20 nm Ni film grown on Si alongside that of a 6 nm QAH insulator grown on Al_2O_3. Reflectivities offset for clarity. Structural and magnetic depth profile used to simulate the reflectivities are shown in (b) for Ni and (c) for the QAHI.

effects. As illustrated in the simulated reflectivity of Fig. 6(a), the critical edge, which corresponds to the point at which total external reflection transitions to partial reflection and transmission, is defined by the largest scattering length density in the multilayer heterostructure. Since this feature is extremely distinct and the measurement uncertainty is generally lowest due to high count rates, the magnetic scattering length density of the highest SLD layer of the stack may generally be easily determined with high confidence.

Unfortunately, the topologically nontrivial layer very rarely defines the critical edge, with typical scattering length density values of a few relevant systems shown in Table II. The most popular magnetic materials with high ordering temperatures, such as Fe, permalloy, or the rare-earth garnets exhibit nuclear SLD values far in excess of the most commonly studied topologically nontrivial systems. It is possible to choose materials with lower nuclear SLD values, but these systems frequently have lower ordering temperatures (EuS) or are antiferromagnetic (CrSb, MnTe). The suitability of these magnetic materials for integration and high-quality growth on the same substrates as the topologically active materials further complicates and limits experimental design. To illustrate this difficulty, Fig. 6 also includes a simulation of the expected reflectivity from a 6-nm-thick layer of $(Bi, Sb)_2Te_3$ with a Cr-dopant level small enough to achieve the QAH effect, where it can be seen that the splitting is smaller and the significant features appear at higher-Q values.

Further complicating the analysis of PNR data is the relative strength of the proximity induced magnetization,

TABLE II. Typical nuclear SLD values associated with a variety of topologically nontrivial materials compared with a series of commonly used magnetic reservoirs in MPE heterostructures [108].

Topological materials	Nuclear SLD (10^{-4} nm^{-2})
Bi_2Se_3	2.83
Sb_2Te_3	2.856
WTe_2	2.084
Bi_2Te_3	1.975
$MnBi_2Te_4$	1.624
Magnetic materials	
Permalloy	9.13
Fe	8.02
$Y_3Fe_5O_{12}$	5.91
CrSb	2.24
EuS	1.53
MnTe	0.42

which is typically thought to be much smaller than that of the neighboring magnetically ordered layer. The prominently used material EuS, for example, has a net magnetization approaching 10^3 emu/cm^3 (1 emu/cm^3 = 1 kA/m) at 5 K, while reported proximity-induced moments are often of the order 30 emu/cm^3 [39,42]. Although the examples discussed here are extreme cases, the combination of small magnetization and low nuclear SLD in the TI layer generally leads to the spontaneously magnetized layer overwhelmingly dominating the splitting between the spin-up and spin-down neutron reflectivities. A rare counterexample is occasionally found in cases where the reservoir of magnetic order is ferrimagnetic or antiferromagnetic, as shown for the case of CrSb/(Bi, Sb)$_2$Te$_3$ in Fig. 7 [36]. Here, while the splitting is extremely small, it arises exclusively from the interface, so that the modeling is highly sensitive to the presence or absence of an MPE [36].

Nevertheless, small changes in the spontaneously ordered magnetic layer, such as an interfacial magnetically dead layer or varying interface roughness, may simulate the effects of

an MPE in the scattering. It then often arises that multiple competing models fit the data equally well, including those with and without an MPE. It is therefore critical to employ secondary techniques such as x-ray reflectivity, electron microscopy, Rutherford backscattering spectroscopy, or atomic force microscopy to constrain or validate parameters such as thickness and interface roughness during the model refinement process. In this way alternative models which fit the data equally well may be eliminated and a model which confirms or eliminates the presence of an MPE may be uniquely identified.

D. X-ray spectroscopy and scattering

Magnetic x-ray spectroscopy offers element-resolved information on the chemical and magnetic properties through spin-polarized photon beams with variable energy [109–111]. In nonmagnetic x-ray absorption spectroscopy (XAS), an incident x-ray photon with an energy corresponding to that of at an elemental absorption resonance is absorbed by the material of interest. This absorption process promotes a core electron of the target element into unoccupied states in vicinity of the Fermi-level or conduction band of the probed material [110,112]. Upon decaying back down from its excited state, the promoted electron releases either an x ray or a photoelectron accompanied by secondary ejected electrons. By scanning the incident photon energy through the elemental absorption edge and analyzing the resultant lineshape, XAS reveals element specific chemical information such as bonding or oxidation state [110,112].

To add sensitivity to element-specific magnetic information, x-ray magnetic circular dichroism (XMCD) measurements are performed by circularly polarizing the incident x-ray beam and probing the changes in XAS spectra with alternating positive and negative magnetic field direction, photon helicity, or a combination of the two [110,111]. The spin-orbit interactions in the core shells of the absorbing electrons, combined with the angular momentum of the absorbed photon, yield spin-dependent excitation of the core electrons
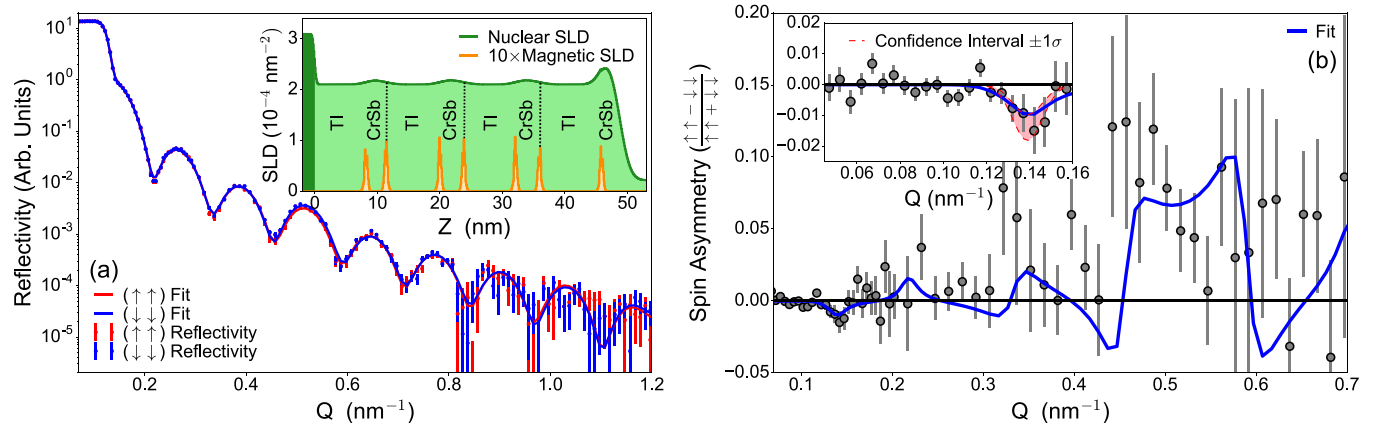

FIG. 7. (a) Neutron reflectivity for the spin-polarized $R^{\uparrow\uparrow}$ and $R^{\downarrow\downarrow}$ channels of a (Bi, Sb)$_2$Te$_3$ superlattice along with (b) spin asymmetry at 6 K with a 700 mT in-plane field. The inset in (a) shows the corresponding model with structural and magnetic SLDs used to obtain the best fit. The inset in (b) exhibits the first dip right after the critical edge. Error bars represent ± 1 standard deviation. From Q. L. He *et al.* (2018) [36].
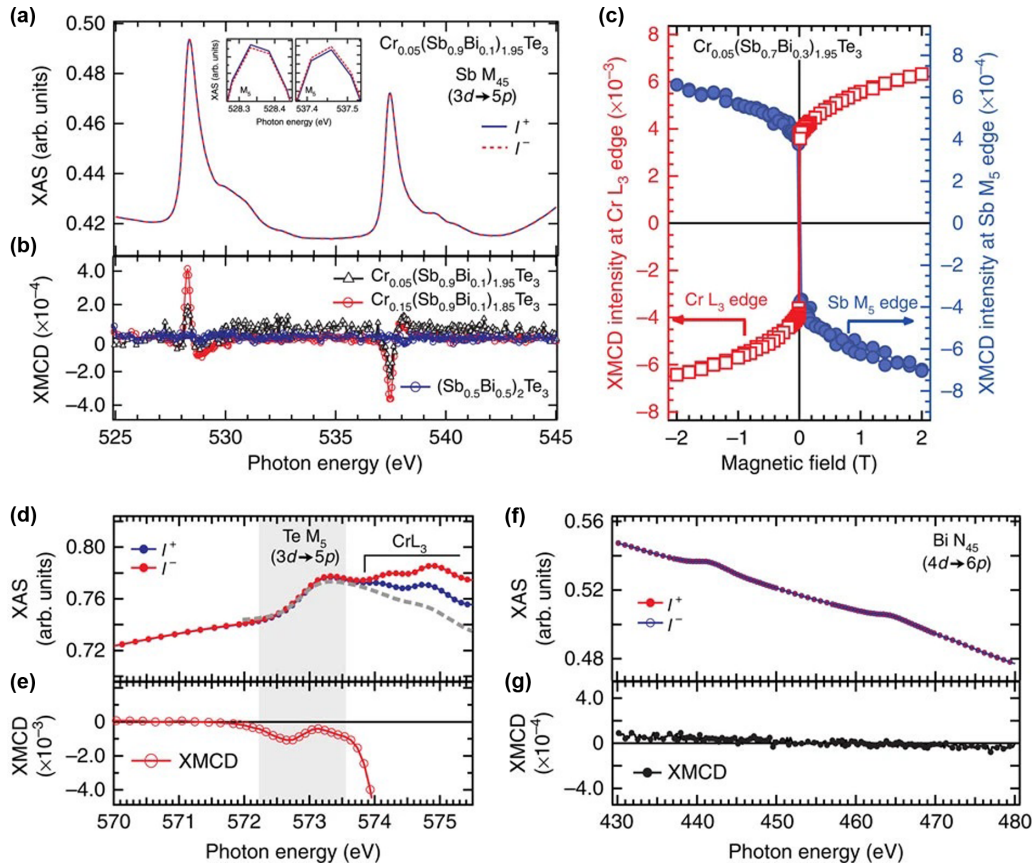
FIG. 8. XMCD study of Cr-doped $(Bi, Sb)_2Te_3$ crystals. (a) XAS and (b) XMCD of the Sb $M_{5,4}$ absorption edge. (c) Comparison between the field-dependent XMCD intensity of the Cr L_3 edge and the Sb M_5 edges. (d) XAS and (e) XMCD of the Te M_5 and part of the Cr L_3 edges. (f) XAS and (g) XMCD at the Bi $N_{5,4}$ edges. Reproduced from M. Ye *et al.*, Nature Comm. **6**, 8913 (2015) [119].

[110,111]. Since the availability of destination states near the Fermi level of a magnetic material is spin-dependent, XMCD allows the magnetic contribution of a given element to be isolated so that the magnetic properties of thin film layers with different compositions can be readily separated [110,111].

Both XAS and XMCD measurements are typically performed in either total electron yield (TEY) mode, in which the charge of the ejected photo- and secondary electrons are measured, fluorescence yield (FY) mode, in which emitted x rays are collected, or luminescence yield (LY) mode, in which the intensity of the x-ray beam passing through a thin film onto a transparent luminescent substrate is detected through a photodiode [113–116]. Each method of data collection has myriad advantages and disadvantages. For example, TEY mode is vulnerable to artifacts related to sample charging and is very surface sensitive but does not suffer from beam depletion or saturation effects [113,114]. On the other hand, FY may probe deeper into the sample but provide more limited signal and altered line shapes resulting from self-absorption or the absorption of significant fractions of the total beam intensity at certain energies [115]. LY avoids both charging and self-absorption issues, but is limited to thin film samples with a maximum thickness and a specific subset of available substrate [116]. Of course, all of these advantages and disadvantages will vary greatly depending on the energies and intensities of the photon beams utilized, which may range from 100s of eV to 10s of keV.

XMCD characterization is commonly employed in complex oxide heterostructures, as in the recent case of $(La, Sr)MnO_3/SrIrO_3$ interfaces which exhibit emergent magnetic properties [117]. This system, which incorporates both magnetic 4d transition metals and high spin-orbit elements, e.g., 6d Ir, provides an excellent example of the challenges inherent in proximity-magnetized TI structures. Specifically, the characteristic photon energies for probing transition elements are generally in the soft x-ray regime of 100–1000 eV, while high spin-orbit materials frequently require energies in excess of 10 keV [118]. Since x-ray spectroscopy beamlines are generally not optimized to access both of these photon energy ranges, one must either attempt to probe transitions with much smaller x-ray interaction cross sections or make measurements at multiple beamlines or x-ray sources.

In spite of these challenges, XMCD has found important applications in doped magnetic TIs and heterostructures, where extremely careful probing of the weak Te $M_{5,4}$, Sb $M_{5,4}$, and Bi $N_{5,4}$ edges has allowed direct comparisons between the dopant and bulk TI magnetizations, as illustrated in Fig. 8 [119–121]. Examples of XMCD-based detection of proximity induced magnetism in TIs, however, are exceedingly rare [41]. While TI-based MPE heterostructures remain even less explored by XMCD than MPEs in general, the field is evolving rapidly. A pair of 2020 studies on the $EuS/(Bi, Sb)_2Te_3$, $Y_3Fe_5O_{12}/Bi_2Te_3$, $Tm_3Fe_5O_{12}/Bi_2Te_3$,
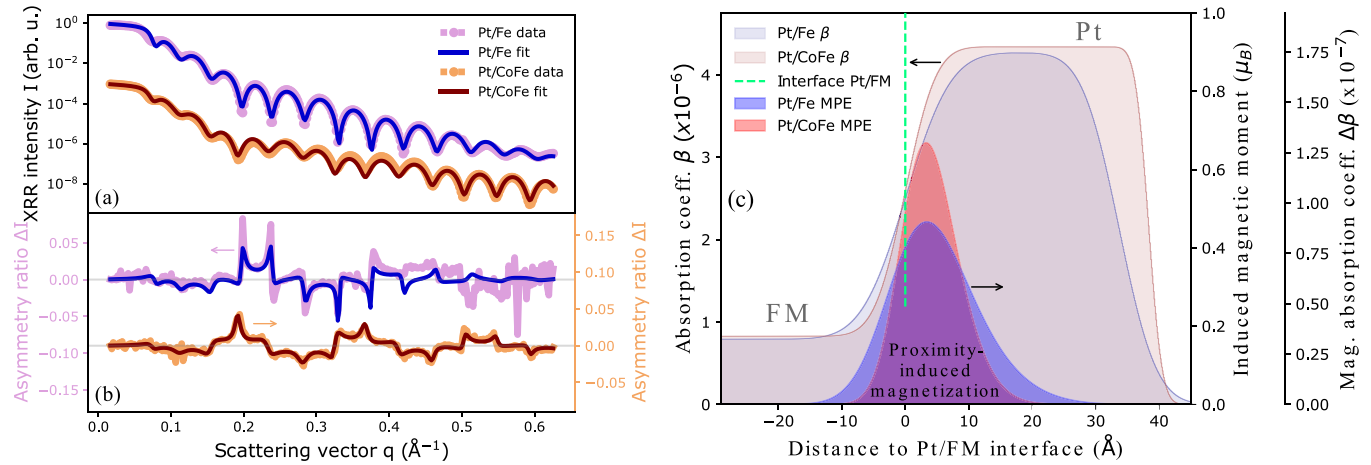
FIG. 9. Fitted (a) resonant reflectivity and (b) asymmetry ratios of XRMR measurements from Pt/Fe and Pt/FeCo heterostructures. (c) Deduced magneto-optic and magnetization depth profiles based on the modeling shown in (a) and (b). Reproduced from D. Graulich *et al.*, Appl. Phys. Lett. **118**, 012407 (2021) [134], with the permission of AIP Publishing.

and Fe_3O_4/Bi_2Te_3 interfaces by Figueroa *et al.* and Pereira *et al.* reported extremely high-precision determination of the upper magnetization limit in this system, suggesting fertile ground in the near future [94,122].

A more recently developed and rapidly maturing technique with the potential to combine the element specificity of x-ray spectroscopy with the depth resolution of polarized neutron reflectometry is x-ray resonant magnetic reflectivity (XRMR). Similarly to PNR, XRMR measures the spin-dependent reflected intensity of a spin-polarized x-ray beam incident on the surface of a thin film heterostructure as a function of the scattering vector Q along the film normal direction [123–125]. Unlike PNR, however, the energy of the x-ray beam may be readily varied to match the resonant absorption edge of specific element in order to isolate the depth-dependent magnetic contribution of that element. By collecting reflectivity curves near the edges of many different elements in the heterostructure, as well as away from any absorption edges, and simultaneously refining the data using a combined model, a comprehensive element specific picture of the depth profile and magnetization can be obtained [126–130]. In addition to dramatically increased intensity relative to PNR measurements, XRMR beamlines can use dramatically smaller spot sizes than neutron scattering measurement so that the sample size and uniformity requirements may be somewhat relaxed. Further, magnetic x-ray scattering factors enable XRMR to access information on both in-plane and growth-axis components of the magnetization [131].

Despite these enormous advantages, XRMR has the disadvantage of extremely complex data analysis, and has been further inhibited by a combination of artifacts including beam-induced surface modifications, energy drift, and strong absorption/saturation effects (among others). However, as modeling and instrumentation has matured, significant improvements have been realized, to the point that extremely accurate quantitative values may now be readily extracted [132,133]. This is particularly true for hard x-ray beamlines, while softer XRMR measurements remain a greater challenge to interpret. In particular, much XRMR work with hard x rays has been recently focused on MPEs in Pt-based

structures in contact with magnetically ordered metals and oxides [82,134,135]. For example, the work of Graulich *et al.* is shown in Fig. 9, where the MPE of Pt interfaced with Fe and CoFe was extracted quantitatively with high precision [134]. While application of this technique to TI heterostructures remains limited, rapid progress may be expected in the near future.

III. PROGRESS IN THE (BI,SB)2(SE,TE)3 MATERIALS FAMILY

The first forays into inducing magnetism in TIs through interfacial coupling were not performed in thin film heterostructures, but rather through a combination of doping and the deposition of magnetic adatoms onto the surface of single crystals. In 2009, Liu *et al.* predicted ferromagnetic interactions between magnetic adatoms on the surface of a TI could be mediated by the topological surface state in the form of an Ruderman-Kittel-Kasuya-Yosida (RKKY) interaction [136]. This magnetic surface interaction was predicted to yield a magnetized state in the TI at the interface and open a gap in the topological surface state. Vobornik *et al.* demonstrated the feasibility of such an approach through the deposition of an Fe overlayer onto the surface of the magnetically doped TI $Bi_{2-x}Mn_xTe_3$, where an enhancement of the magnetic ordering temperature was observed through XMCD on the Mn $L_{2,3}$ edges [137,138]. From this point, efforts evolved rapidly to incorporate a wide range of thin-film heterostructures as TI thin film quality improved and appropriate magnetic reservoir materials were identified for heteroepitaxy. In this section, we will examine in detail the progress made in the most widely studied material families used as reservoirs of magnetic order in TI heterostructures.

A. EuS and other rare earth interfaces

By 2013, inroads were made towards identifying MPEs in thin film heterostructures of undoped TIs. Wei *et al.* identified the low-temperature Heisenberg ferromagnetic insulator EuS as a promising candidate with the key features for thin film magnetotransport characterization—low conductivity, growth
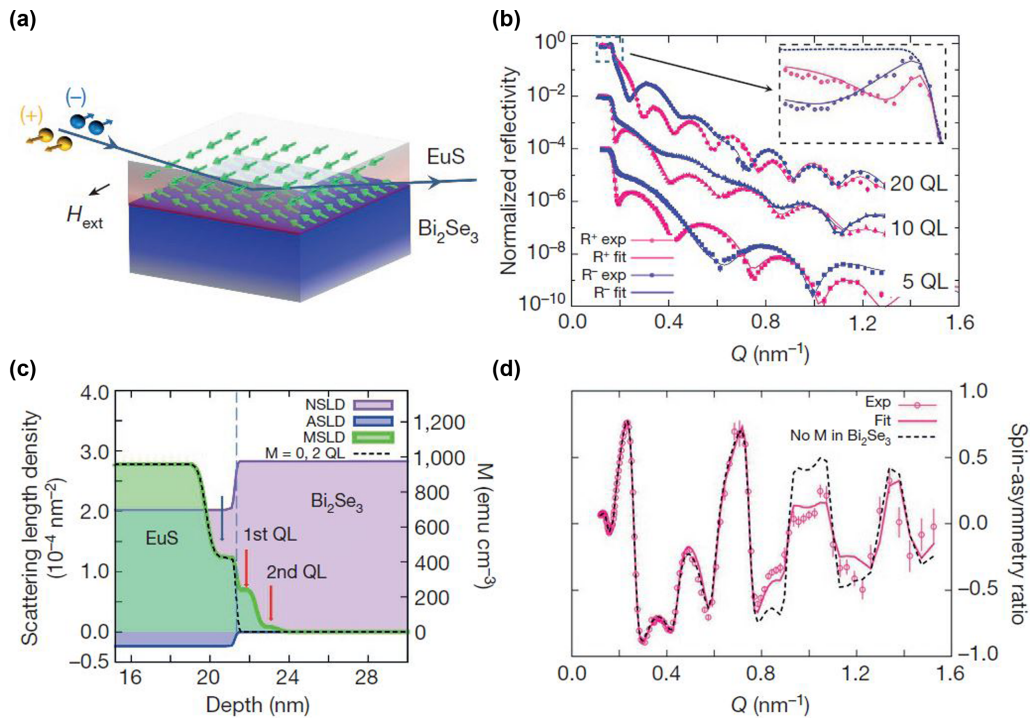
FIG. 10. PNR study of the EuS/Bi$_2$Se$_3$ interface (a) Schematic of the Bi$_2$Se$_3$/EuS bilayer and PNR experimental geometry alongside magnetic depth profile interpretation by Katmis *et al.* [39]. (b) Fitted PNR for a series of Bi$_2$Se$_3$/EuS with varying Bi$_2$Se$_3$ thickness in units of quintuple layers (QLs). (c) Magnetic, nuclear, and absorption SLD profiles used to fit the 20 QL sample shown in (b) at 5 K. (d) Spin asymmetry of the 20 QL data alongside theoretical fit from model in (c) and a counterfactual simulation with zero magnetization in the two layers marked "1st QL" and "2nd QL." Error bars represent ±1 standard deviation. Reprinted by permission from Springer Nature Customer Service Centre GmbH: Springer Nature, Nature, A high-temperature ferromagnetic topological insulating phase by proximity coupling, F. Katmis *et al.*, Copyright Springer Nature (2016), https://www.nature.com/ [39].

compatibility with Bi$_2$Se$_3$, and a large magnetic moment of nearly 7 μ_B/Eu [38]. Although the work of Wei *et al.* was primarily based upon bulk magnetometry and magnetotransport characterization, later work by Li *et al.* and Katmis *et al.* incorporated detailed polarized neutron reflectometry measurements [39,139].

Even eight years later, the coupling between EuS and the (Bi, Sb)$_2$(Se, Te)$_3$ family of TIs remains complex and relatively poorly understood, in part due to the combination of strong perpendicular and in-plane anisotropy associated with the TI and EuS layers, respectively. Ferromagnetic/antiferromagnet type coupling has been reported between EuS and ferromagnetic V-doped Sb$_{2-x}$V$_x$Te$_3$ while an exchange-spring type interface canting is suggested at the EuS/Bi$_2$Se$_3$ interface [39,139].

Interestingly, PNR results on EuS-interfaced Sb$_2$Te$_3$, (Bi$_{0.2}$, Sb$_{0.8}$)$_2$Te$_3$ and Bi$_2$Se$_3$ (Fig. 10) differ significantly, with proximity induced magnetizations ranging from approximately 75 emu/cm^3 to 120 emu/cm^3 and 240 emu/cm^3, respectively [39,139,140]. It should be noted that some of these values are surprisingly large when compared to MPE values measured in multilayers of 1-nm-thick Pt interfaced with Ni or Co at 10 K, which ranged from 120 emu/cm^3 to 430 emu/cm^3 [141–144]. The temperature dependence of MPEs induced by EuS is also the subject of a variety of conflicting reports, with polarized neutron reflectometry and the optically based magnetic second harmonic generation (MSHG) techniques yielding widely different results.

While the EuS/Bi$_2$Se$_3$ system was the first reported example of a near room-temperature MPE in an undoped TI, MSHG measurements on similar samples yielded an upper limit of approximately 17 K, the bulk transition temperature of EuS [39,40,145]. A relatively recent report attempted to resolve this ambiguity through the application of low-energy muon spin rotation measurements, finding clear evidence of a large MPE activating at 17 K and ambiguous evidence of a temperature-dependent signal above 17 K which could indicate higher-temperature magnetism but was also present in a EuS/Ti control sample [146]. The element-specific XMCD measurements shown in Fig. 11, on the other hand, yielded no evidence of any MPE even at 3 K, with an upper limit to the proximity-induced magnetization at least 2 orders of magnitude lower than previous PNR reports [122]. In this case, the authors speculate that Eu migration into the TI may explain many of the observations in the literature. Indeed, during MBE growth of epitaxial EuS/Bi$_2$Se$_3$, the Eu and S fluxes impinging on the Bi$_2$Se$_3$ thin film substrate may readily lead to Eu and S substitution for Bi and Se, respectively. This can be understood in terms of the increased reactivity of Eu and S compared to Bi and Se. Several experimental and theoretical studies have demonstrated Eu incorporation into Bi$_2$Se$_3$ and Bi$_2$Te$_3$ along with evidence of associated dopant-induced magnetic order [147–149].

Further illustrating the degree to which rare-earth elements may be incorporated into TI films such as (Bi, Sb)$_2$Te$_3$ and yield exotic magnetic states is the work exploring
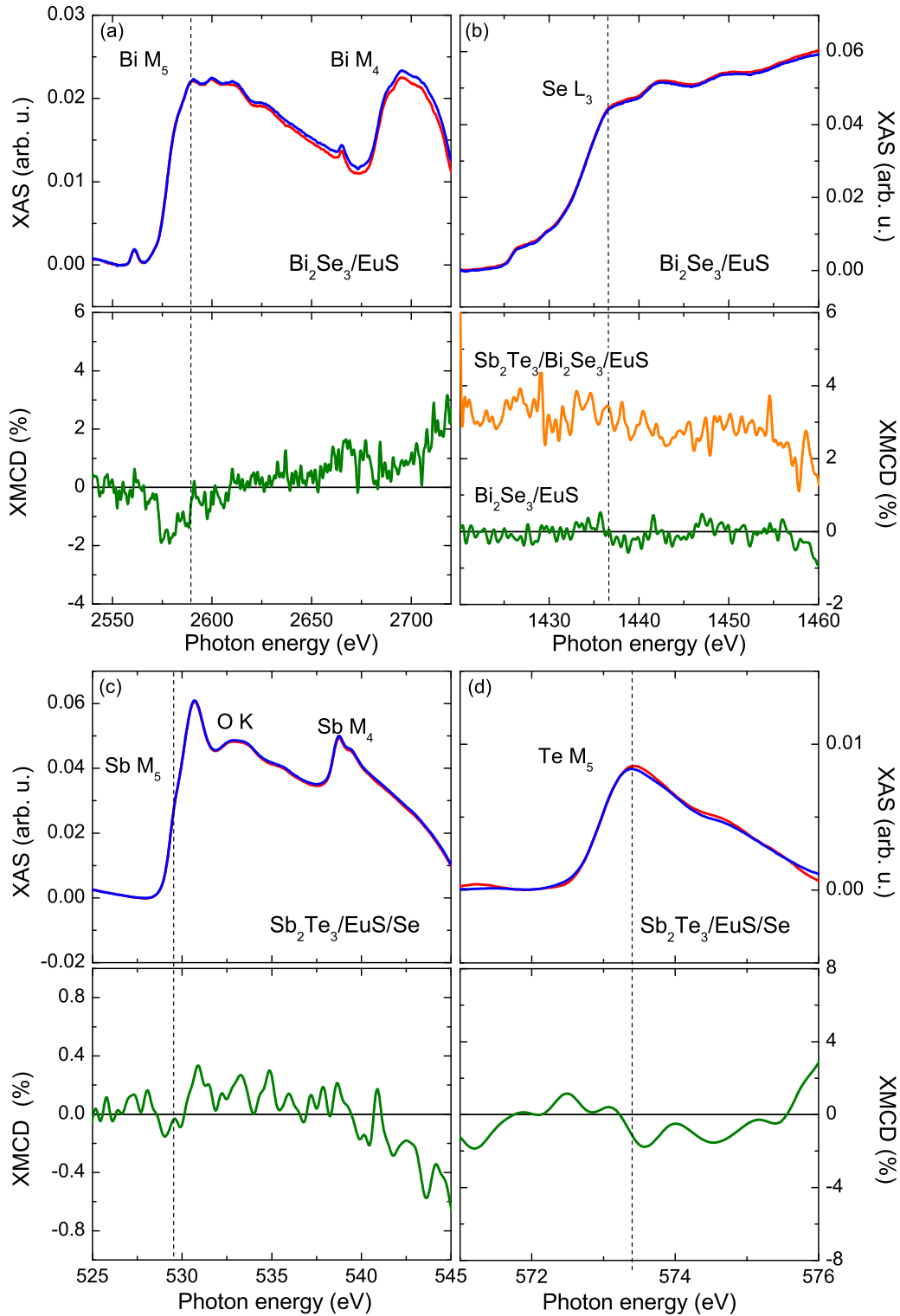
FIG. 11. XAS/XMCD study of the Bi_2Se_3/EuS and Sb_2Te_3/EuS interfaces. XAS and XMCD at (a) the Bi $M_{5,4}$ edges, (b) the Se L_3 edge, (c) the Sb $M_{5,4}$ edges, and (d) the Te M_5 edge. No significant proximity-induced XMCD was observed. From A. I. Figueroa *et al.* (2020) [122].

proximity and interface coupling between Dy-doped Bi_2Te_3 and Cr-doped Sb_2Te_3 [97,121,150]. Not only do PNR, XMCD, transport, and magnetometry studies show that proximity coupling to Cr:Sb_2Te_3 may induce a net magnetization in the Dy:Bi_2Te_3, but exchange bias may also be observed due to the antiferromagnetic coupling across the Dy:Bi_2Te_3/Cr:Sb_2Te_3 interface [97,121,150]. In superlattices of Dy:Bi_2Te_3/Cr:Sb_2Te_3, a 60 K enhancement of the T_C is also observed [97]. Direct substitution of rare-earth elements into the TI may clearly be used to obtain both strong interface coupling and emergent magnetic states in these heterostructures.
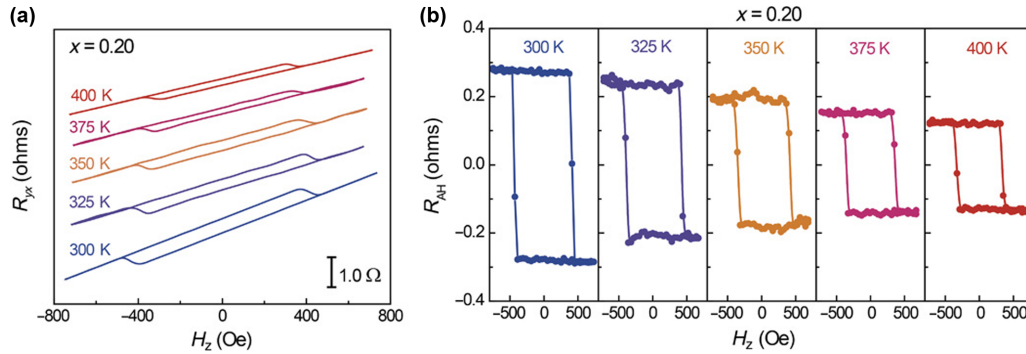
FIG. 12. (a) Temperature-dependent Hall resistance from a TmIG/(Bi$_x$Sb$_{1-x}$)$_2$Te$_3$ heterostructure (b) Data from (a) after subtraction of the ordinary linear Hall effect. A clear hysteresic AHE can be observed across the entire temperature range. Figure adapted from C. Tang *et al.*, Sci. Adv. **3**, e1700307 (2017) [26].

A great deal of additional work is clearly necessary in order to robustly understand these complex systems, as it remains unclear whether the wide disparity in results are related to sample variation, differences in probe sensitivity, or the placement of the Fermi level with respect to the surface Dirac cone in different members of the (Bi, Sb)$_2$(Se, Te)$_3$ family.

B. Insulating oxides

The rare earth iron garnets are well known and widely studied as highly insulating ferrimagnets, with particular interest devoted to Y$_3$Fe$_5$O$_{12}$ (YIG) for desirable properties such as long magnon lifetimes associated with ultra-low magnetic damping [151–155]. Consequently, YIG has been extensively explored for spin-pumping applications in thin films [156–159]. In these studies, evidence of the MPE emerged in YIG/Pt bilayers so that these rare-earth garnets represent appealing platforms for the realization of MPEs in topological matter, although the existence, strength, and onset temperature of the MPE remains the subject of debate [68,158,160–162]. Unlike in Pt, the strong perpendicular anisotropy which emerges in TIs such as (Bi, Sb)$_2$Te$_3$ when they are magnetized complicates the interfacial interactions, so that magnetic insulators with both in-plane and perpendicular anisotropy are of interest. Thus garnets with varying anisotropy such as Tm$_3$Fe$_5$O$_{12}$ (TmIG), Eu$_3$Fe$_5$O$_{12}$, and Tb$_3$Fe$_5$O$_{12}$ have also been studied extensively [163,164].

The vast majority of MPEs reported in the YIG/TI system are characterized primarily through magnetotransport measurements such as the AHE or spintronic measurements such as FMR [27,89,94,165–167]. The observed R_{xy} in AHE measurements of these, and other iron garnet-based systems, is typically quite small, ranging between 10^{-1} Ω to 10^1 Ω at low temperature. Despite the extensive study, even basic information about YIG/TI heterostructures, such as the direction and magnitude of the induced magnetization at the interface, remains unclear. For example, there are many conflicting reports about the complex coupling reported at the YIG/TI interface, with Lang *et al.* reporting antiparallel coupling between the magnetization and MPE in a MOKE magnetization study while others have reported ferromagnetic coupling across the interface for both undoped and Cr-doped TI layers [28–30,89,168]. It has even been reported recently by Liu *et al.* that the modification of the magnetic ground state

does not exclusively flow from YIG to the TI layer, but that topological surface states in Bi$_2$Se$_3$ modify the magnetism in the adjacent YIG as well [169].

It is particularly interesting to note that while the garnets studied generally have ordering temperatures in excess of 300 K, the reported Curie temperature of proximity-induced magnetization within the TI is typically significantly suppressed and varies widely, from 30 K to 180 K [27,30,89,167]. The TmIG/(Bi, Sb)$_2$Te$_3$ system has been reported to exhibit an anomalous Hall effect up to 400 K (see Fig. 12), with point-contact Andreev reflectivity indicating spin polarization of the TI at 1.5 K [26]. However, later XMCD measurements on the same system (shown in Fig. 13) found strong dichroism on the Te M$_{5,4}$ edge at 20 K which decayed below detectable levels between 90 and 200 K, leaving the onset temperature of proximity induced magnetization, as well as the relative contributions of the MPE and spin-Hall effect, in TmIG/(Bi, Sb)$_2$Te$_3$ somewhat ambiguous [94,170].

Although garnets are likely the most widely studied reservoirs of magnetic order in TI-based heterostructures, numerous other insulating magnetic complex oxide systems such as barium hexaferrite (BaFe$_{12}$O$_{19}$), LaCoO$_3$, and Fe$_3$O$_4$ have been investigated. In the case of the insulating ferromagnet LaCoO$_3$, the limited number of extant studies are primarily based on magnetometry and transport measurements. Zhu *et al.* report the observation of an anomalous Hall effect
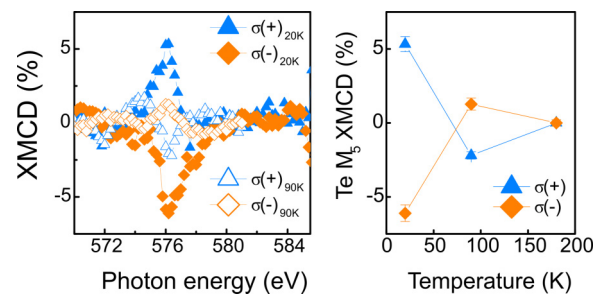

FIG. 13. (left) Te M$_5$ edge XMCD asymmetry from a TmIG/(Bi, Sb)$_2$Te$_3$ heterostructure at 20 K and 90 K after field cooling. (right) Peak Te XMCD asymmetry in this sample as a function of temperature. Error bars represent ±1 standard deviation. Reproduced from C.-Y. Yang *et al.*, Appl. Phys. Lett. **114**, 082403 (2019) [170], with the permission of AIP Publishing.

signal and the suppression of weak antilocalization as signatures of induced ferromagnetism in an adjacent Bi_2Se_3 film [33]. Surprisingly, a significant anomalous Hall signal appears to persist well above the 85 K Curie temperature of $LaCoO_3$, being present above 100 K. The authors attribute this to enhanced interfacial ferromagnetism induced by spin-orbit interactions at the TI interface [33]. Recent work on Fe_3O_4/Bi_2Te_3 heterostructures also noted both weak antilocalization suppression and a nonlinear feature in the AHE, potentially indicating MPE-induced gap opening in this system [94]. XMCD measurements on the Te edge of a single quintuple layer of Bi_2Te_3 on Fe_3O_4 revealed no net dichroism within measurement uncertainty, indicating that any MPE is extremely weak [94].

As can be seen, the dominance of transport measurements in insulating oxides has led to a great deal of ambiguity regarding the relative contributions of static and nonequilibrium (i.e., current induced) proximity effects in these systems. One of the best examples of this is the barium hexaferrite system. Though $BaFe_{12}O_{19}$/TI heterostructures have been studied since 2014, characterization remains almost exclusively transport-based [31,32]. As in $LaCoO_3$, weak antilocalization suppression and a nonzero anomalous Hall resistance of up to 10^{-2} Ω is reported in this system across a wide temperature range [31,32]. Nevertheless, no direct interfacial magnetization measurements have been reported and the question of a static vs. current induced signal remain open several years later [171]. A critical complicated factor is the likely necessity of a vacuum break in the sample preparation process. Since the thin film oxide substrates are generally prepared by magnetron sputtering or pulsed laser deposition techniques, the film sample is generally unloaded from the vacuum chamber to ambient air and transfer into another vacuum system for the deposition of TI. Such an *ex situ* process may lead to significant challenges in establishing consistent interface quality by introducing many uncontrolled factors in heterostructure fabrication.

C. Antiferromagnet-based structures

As an alternative to magnetically ordered systems with a net magnetization, efforts to induce MPEs in TIs through coupling to antiferromagnets emerged in 2017. The NiAs family of antiferromagnets, including CrSb, MnTe, and CrSe, is particularly promising due to a structure which allows for high-quality growth alongside $(Bi, Sb)_2Te_3$ and similar materials in bilayers or even superlattices. These hexagonal systems have tunable properties ideal for exploring interfacial exchange coupling, typically comprising ferromagnetically ordered basal planes with antiferromagnetic coupling along the c-axis, so that local areas may encounter spin-polarized regions across the interface which may mimic ferromagnetic order. In this sense, antiferromagnetic proximity effects rely on the extraordinarily local interactions associated with orbital overlap and exchange coupling across the interface. Of further interest is the tunable Néel order which allows for varying interactions between the antiferromagnet and TI. CrSb and MnTe, for example, have nearly identical A-type antiferromagnet orders with the exception that CrSb spins align along the c-axis while MnTe spins lie within the *ab* basal plane
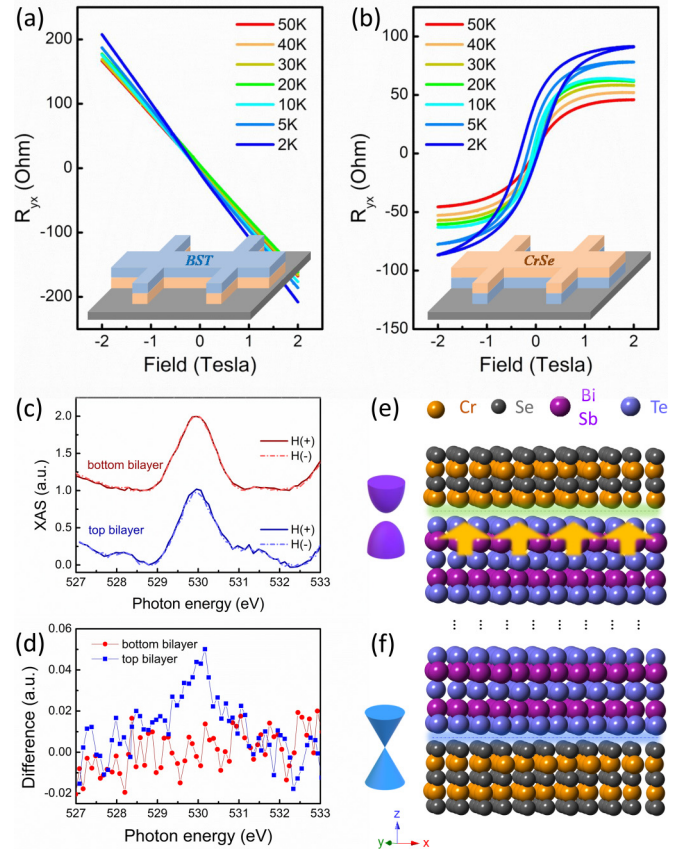

FIG. 14. Temperature dependence of R_{xy} vs applied magnetic field for (a) CrSe/$(Bi, Sb)_2Te_3$ (bottom) and (b) $(Bi, Sb)_2Te_3$/CrSe (top) bilayers. Low-temperature Sb M_5-edge (c) XAS and (d) XMCD for CrSe/$(Bi, Sb)_2Te_3$ (bottom) and $(Bi, Sb)_2Te_3$/CrSe (top) bilayers alongside schematics representing changes in termination for (e) $(Bi, Sb)_2Te_3$/CrSe (top) and (f) CrSe/$(Bi, Sb)_2Te_3$ (bottom) bilayers. Figure adapted from C.-Y. Yang *et al.*, Sci. Adv. **6**, eaaz8463 (2020) [41].

[172–175]. CrSe instead exhibits an umbrella-type noncolinear antiferromagnetic order which resembles a modified A-type [176,177].

In 2017, superlattices of CrSb and Cr-doped $(Bi, Sb)_2Te_3$ were shown to yield a dramatic enhancement of the magnetic ordering temperature within the magnetic TI layers, along with the establishment of modified spin texture in the CrSb and long-range interlayer exchange coupling. These findings were the first indication that a MTI could couple strongly with an antiferromagnetic layer [35]. Shortly thereafter, a net magnetization was observed in related superlattices of CrSb and undoped $(Bi, Sb)_2Te_3$, resulting in a series of topological phase transitions attributed to MPEs at the top and bottom TI interfaces [36]. Proximity effects stabilized through interfacing with CrSe and MnTe have also been reported. Of particular interest is the case shown in Fig. 14, where transport, PNR, and XMCD measurement reveal that the signatures of MPEs in CrSe are highly termination dependent, with Se termination destroying the interface coupling [41]. MnTe, on the other hand, has been reported to exhibit signatures of both a MPE and noncolinear spin textures due to the combination of strong

out-of-plane anisotropy in the TI layer with the in-plane spins of MnTe [42]. On the other hand, recent evidence suggests that these signatures may instead arise as a result of multiphase interface magnetism [178].

The signatures of MPEs in NiAs-based TI heterostructures have been probed by a wide variety of techniques, including magnetometry, magnetotransport, PNR, and XMCD. In contrast to other ferromagnet or ferrimagnet-based heterostructures, a significant majority of the total magnetic moment within antiferromagnet-TI structures appears to originate at the interface. This moment may be attributed either to uncompensated spins at the antiferromagnet surface, a net induced magnetization within the TI, or some combination of the two. Regardless, antiferromagnetic systems appear to offer a unique opportunity to precisely localize the characterized magnetization at the interface. Of further note is the reported R_{xy}, which ranges from 10^0 Ω to 10^4 Ω, significantly larger than that of, for example, garnet-based structures. However, the significance of such large R_{xy} values is difficult to determine, as much of the current appears to shunt through the antiferromagnetic layers, which may be either highly conductive (CrSb, MnTe) or relatively insulating (CrSe).

Interface coupling between antiferromagnets and TIs is not limited to NiAs-type systems. Although not an example of an induced MPE, exchange coupling has been demonstrated in the well-known oxide magnetoelectric antiferromagnet Cr_2O_3 [43,44,179]. Wang *et al.* reported an antiferromagnetic coupling between Cr_2O_3 while Pan *et al.* found exchange bias in Cr-doped $(Bi, Sb)_2Te_3$ grown on Cr_2O_3 [44]. Although the TI layers in both studies were magnetized through Cr-doping rather than an MPE, Cr_2O_3 has been identified as one of the only magnetically ordered systems in which both the QAHE and interfacial exchange coupling have been demonstrated. Coupled with the known magnetoelectricity in Cr_2O_3, this system represents a promising platform for tunable quantum states in magnetic TIs.

D. Telluride-based heterostructures

Layered Van der Walls tellurides were among the first materials in which magnetic proximity coupling in TI films has been reported [45]. In 2014, Alegria *et al.* reported epitaxy of Bi_2Te_3 on single crystals of the layered Van der Waals material $Cr_2Ge_2Te_6$. $Cr_2Ge_2Te_6$ is in many ways an ideal candidate for the formation of high-quality interfaces with the $(Bi, Sb)_2(Se, Te)_3$ family, possessing a hexagonal crystal structure which is a relatively good lattice match and a Te-termination layer which may favor Te/Se-terminated growth of the adjacent TI. Given the reported importance of direct orbital overlap between the spin-polarized electron wave functions of magnetically ordered atoms and the topological surface states, it remains unclear whether the Te-termination may be expected to reduce the magnitude of any induced MPE even as it facilitates growth. $Cr_2Ge_2Te_6$ is also convenient for magneto-transport measurements due to the low-temperature combination of c-axis oriented ferromagnetism and high resistivity which may limit current shunting through the magnetically ordered layer. Early studies on this system consequently focused heavily on the anomalous Hall

effect, where large R_{xy} values exceeding 10^3 Ω have been reported [45–47].

While the initial studies involved growth of TI films on single crystal telluride substrates, a 2019 study by Mogi *et al.* examined thin film $Cr_2Ge_2Te_6/(Bi, Sb)_2Te_3/Cr_2Ge_2Te_6$ sandwich heterostructures grown by molecular beam epitaxy. In addition to anomalous Hall measurements, PNR measurements were performed and suggested than any induced magnetization in the TI layer is below 20 emu/cm^3 [47]. These results were also consistent with zero net magnetization. It is of additional interest that varying the Bi/Sb ratio in these sandwich structures revealed evidence of passing through the charge neutral point, indicating strong transport contributions from the topological surface states. The authors further note that the peak σ_{xy} value of $0.2e^2/h$ appears at the most resistive sample [47]. Nevertheless, direct evidence of a net magnetization induced by a static MPE remains elusive, and it is suggested that surface state penetration into the $Cr_2Ge_2Te_6$ may play a signficant role.

Lastly, we turn to the closely related $Zn_{1-x}Cr_xTe/(Bi_ySb_{1-y})_2Te_3/Zn_{1-x}Cr_xTe$ sandwich structures, the lone reported example of a proximity induced QAH insulator. In 2019, Watanabe *et al.* reported on all-telluride thin film sandwich heterostructures incorporating the doped insulating ferromagnet $Zn_{1-x}Cr_xTe$ and the TI $(Bi_ySb_{1-y})_2Te_3$, where the composition of $x = 0.60$ has been selected for proximity of the Fermi level to the charge neutral point and exchange gap opened through proximity coupling [48]. As shown in Fig. 15, the QAH effect is successfully realized at the charge neutral point in this heterostructure, with a R_{xy}^A of h/e^2. By tuning the composition further, Watanabe *et al.* find a sharp peak in the anomalous Hall resistance, which decreases by 1–2 orders of magnitude as the composition is tuned away from the charge neutral point. These findings represent a strong indication that much of the spread in reported R_{xy}^A may be explained in terms of Fermi level position and defect conduction pathway density in the TI layer.

As revealed by spectroscopy measurements and first-principle calculations for the magnetic TI, Cr-, and V-doped $(Bi, Sb)_2Te_3$, the energy levels of the spin polarized density of states for the 3D magnetic elements are close to the $5p$ orbitals of Te [180,181]. This orbital configuration can produce large overlap, leading to a wide exchange gap in the topological surface states. This may at least partially explain the QAHE observed in $Zn_{1-x}Cr_xTe/(Bi_ySb_{1-y})_2Te_3/Zn_{1-x}Cr_xTe$, as strong hybridization may occur between the p orbital of Te from the TI and the d-orbital from the adjacent magnetic insulator. Despite this exciting progress, it must be noted that the 100 mK quantization temperature remains far below the 60 K T_C of the adjacent $Zn_{1-x}Cr_xTe$. In this case, the small effective exchange gap has been attributed to an inhomogeneous exchange gap across the entire surface of the TI layer induced by random Cr dopants in both ZnTe layers, similar to the inhomogeneity observed in Cr-doped $(Bi, Sb)_2Te_3$ [48,57]. These results show that all-telluride heterostructures can be a successful pathway towards MPE-induced QAH insulators, increasing exchange gap homogeneity and magnitude will require a great deal of additional effort.
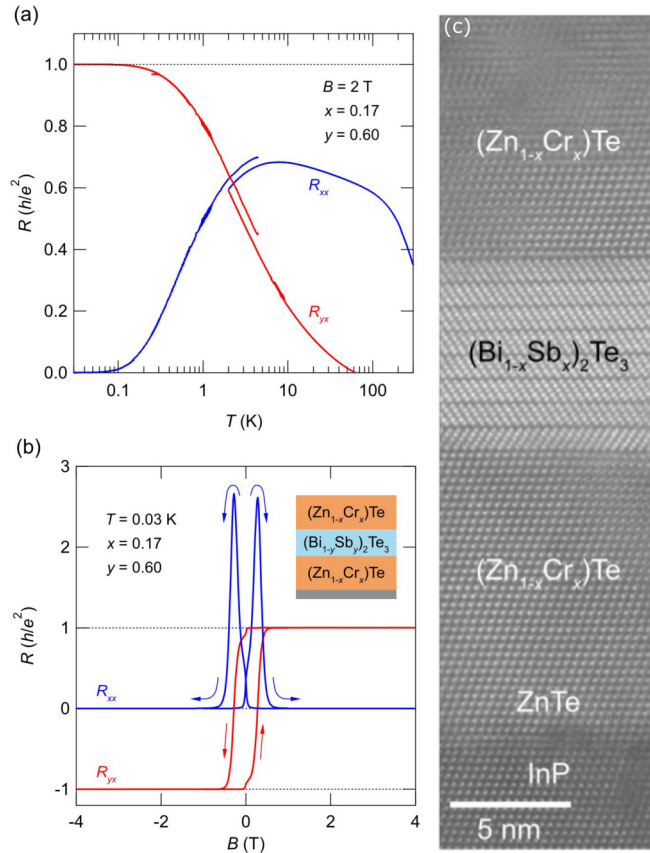
FIG. 15. (a) R_{xx} and R_{yx} vs T and R_{xx} and R_{yx} vs applied magnetic field for a $(Bi, Sb)_2Te_3$ film sandwiched by $(Zn,Cr)Te$. (c) High-resolution cross-sectional scanning transmission micrograph of a $(Bi, Sb)_2Te_3$ film sandwiched by $(Zn,Cr)Te$. Reproduced from R. Watanabe *et al.*, Appl. Phys. Lett. **115**, 102403 (2019) [48], with the permission of AIP Publishing.

IV. SUMMARY AND OUTLOOK

In this progress report, we have examined the recent efforts towards inducing an exchange gap and net magnetization in TIs through interfacing with a reservoir of magnetic order, with particular emphasis on the methods for characterizing MPEs at the interfaces. While enormous progress has been made and magnetic proximity-induced realization of the QAH effect has been demonstrated, the central goal of increasing the quantization temperature remains elusive. Further, a great deal of ambiguity remains in the literature, with nominally similar systems exhibiting everything from widely disparate temperature dependencies to even disagreement regarding the presence or absence of any MPE at all.

Of particular concern is the tendency for disagreement between measurements performed by different techniques. Some inconsistency between transport measurements is to be expected given the combination of extreme sensitivity to the interface scattering and the multiple alternative mechanisms for inducing an apparent anomalous Hall signal which are unrelated to a static MPE. However, even measurements by nominally direct depth or element-resolved techniques often appear contradictory. In the EuS/TI interfaces, for example, XMCD and PNR measurements show no proximity-induced

magnetization and an interfacial magnetization of several hundred emu/cm^3, respectively. Such values are well-within the detection limits of either technique.

While this review focuses mainly on the magnetic characterization of MPEs in TI-based heterostructures, we must note that magnetic characterization does and should not occur outside of the context provided by precise structural information. TIs and other topologically nontrivial materials are often structurally complex, prone to defects, and may be influenced by either the quality or chemistry of the interface. In the face of such disparate results in the literature, is it critical to ensure that interface structures are well characterized in order to legitimately compare results across studies. There is consequently a clear need for spectromicroscopies such as electron energy loss spectroscopy and high-precision imaging such as four-dimensional scanning transmission electron microscopy, which combines imaging with position sensitive electron diffraction [24,182,183]. Emerging techniques which combine real-space structural information with magnetic sensitivity, such as electron magnetic circular dichroism or differential phase contrast electron microscopy may also provide key information [184–186].

In addition to resolving the characterization challenges, much progress remains to be made in the design of heterostructures which can maximize a uniform exchange gap at both the top and bottom surfaces of the TI. To further enhance the MPE for TIs, the following questions remain to be addressed:

(1) **Interface termination and quality:** Magnetic atoms (usually metallic ions) in many magnetic materials are frequently sandwiched by nonmagnetic layers at both surfaces, e.g., Te-Mn-Te in MnTe. Even materials with surfaces terminated by ordered spins may be passivated or oxidized by nonmagnetic species, e.g., Te or O ions, which may occur in *in situ* Te-rich growth environments and *ex situ* hetero-epitaxy, respectively. Without direct contact, the spin polarization of the magnetic ions may have a dramatically reduced effect on the topological surface states.

(2) **Orbital structure:** The MPE mainly originates through interfacial orbital overlap and hybridization, where the electronic structure of the magnetic atoms alters either the conduction or valence band of the nonmagnetic material. Therefore, to enhance the MPE, band alignment and increased orbital overlap between the electronic states of magnetic atoms and the topological surface states should be maximized.

(3) **Magnetic exchange mechanism:** Two possible exchange mechanisms are considered to be the origin of magnetism in TIs. Firstly, it was experimentally found in Mn-doped $Bi_2Te_{3-y}Se_y$ that both the Hall conductance and T_C are enhanced along with the decrease of the carrier density when the Fermi level approaches the exchange gap [25,187]. Such behavior implies that the topological surface states may mediate exchange coupling among magnetic ions through RKKY type interactions [136,188]. However, the maximum T_C appears when the Fermi level is at the Dirac point. This can also be understood in terms of the maximization of the energy gain for Dirac electrons due to the opening of the exchange gap, similar to the Peierls transition, or in terms of the spin–spin interactions mediated by the bulk valence band [136]. In the Cr-doped $(Bi, Sb)_2Te_3$ system, it was surprisingly found that

T_C is almost independent of the carrier type or density, which is in sharp contrast to Mn-doped TIs [23]. allowed in text. Move to references per journal requirements. Such behavior is suggestive of the Van Vleck mechanism, which is induced by 3D transition metal dopants, e.g., Cr [189,190]. The complex origin of magnetic order in TI requires further theoretical and experimental investigations.

It is clear therefore that much work remains to be done, and that reliable interpretation of results requires the application of a wide range of characterization techniques to any given system. Nevertheless, as the quality of TI-based interfaces and heterostructures continues to increase and maturing techniques such as XRMR are applied, it is likely that the field will begin to converge. In particular, large scale growth of the highly promising all-telluride structures remains in its infancy and may enable significant strides in coming years. Improvements in interface termination and quality control will likely enable stronger orbital overlap and increased homogeneity so that the exchange gap will be both larger and more uniform. In this way, proximity-induced magnetic order in TIs may yet prove to be a realistic gateway towards high-temperature QAH insulators and real-world implementation of lossless quantum devices.

[1] M. Z. Hasan and C. L. Kane, Rev. Mod. Phys. **82**, 3045 (2010).

[2] J. E. Moore, Nature (London) **464**, 194 (2010).

[3] M. König, S. Wiedmann, C. Brüne, A. Roth, H. Buhmann, L. W. Molenkamp, X.-L. Qi, and S.-C. Zhang, Science **318**, 766 (2007).

[4] Q. L. He, L. Pan, A. L. Stern, E. C. Burks, X. Che, G. Yin, J. Wang, B. Lian, Q. Zhou, E. S. Choi, K. Murata, X. Kou, Z. Chen, T. Nie, Q. Shao, Y. Fan, S.-C. Zhang, K. Liu, J. Xia, and K. L. Wang, Science **357**, 294 (2017).

[5] J. Shen, J. Lyu, J. Z. Gao, Y.-M. Xie, C.-Z. Chen, C.-W. Cho, O. Atanov, Z. Chen, K. Liu, Y. J. Hu, K. Y. Yip, S. K. Goh, Q. L. He, L. Pan, K. L. Wang, K. T. Law, and R. Lortz, Proc. Natl. Acad. Sci. USA **117**, 238 (2020).

[6] S. Wang, B.-C. Lin, A.-Q. Wang, D.-P. Yu, and Z.-M. Liao, Adv. Phys.: X **2**, 518 (2017).

[7] I. Crassee, R. Sankar, W.-L. Lee, A. Akrap, and M. Orlita, Phys. Rev. Mater. **2**, 120302 (2018).

[8] B. Yan and C. Felser, Annu. Rev. Condens. Matter Phys. **8**, 337 (2017).

[9] Y. Ando and L. Fu, Annu. Rev. Condens. Matter Phys. **6**, 361 (2015).

[10] B. Yan and S.-C. Zhang, Rep. Prog. Phys. **75**, 096501 (2012).

[11] K. He, Y. Wang, and Q.-K. Xue, Annu. Rev. Condens. Matter Phys. **9**, 329 (2018).

[12] Y. L. Chen, J. G. Analytis, J.-H. Chu, Z. K. Liu, S.-K. Mo, X. L. Qi, H. J. Zhang, D. H. Lu, X. Dai, Z. Fang, S. C. Zhang, I. R. Fisher, Z. Hussain, and Z.-X. Shen, Science **325**, 178 (2009).

[13] Y. Tanaka, Z. Ren, T. Sato, K. Nakayama, S. Souma, T. Takahashi, K. Segawa, and Y. Ando, Nat. Phys. **8**, 800 (2012).

[14] C.-Z. Chang, J. Zhang, X. Feng, J. Shen, Z. Zhang, M. Guo, K. Li, Y. Ou, P. Wei, L.-L. Wang, Z.-Q. Ji, Y. Feng, S. Ji, X. Chen, J. Jia, X. Dai, Z. Fang, S.-C. Zhang, K. He, Y. Wang *et al.*, Science **340**, 167 (2013).

[15] B. Q. Lv, H. M. Weng, B. B. Fu, X. P. Wang, H. Miao, J. Ma, P. Richard, X. C. Huang, L. X. Zhao, G. F. Chen, Z. Fang, X. Dai, T. Qian, and H. Ding, Phys. Rev. X **5**, 031013 (2015).

[16] L. X. Yang, Z. K. Liu, Y. Sun, H. Peng, H. F. Yang, T. Zhang, B. Zhou, Y. Zhang, Y. F. Guo, M. Rahn, D. Prabhakaran, Z. Hussain, S.-K. Mo, C. Felser, B. Yan, and Y. L. Chen, Nat. Phys. **11**, 728 (2015).

[17] Z. K. Liu, B. Zhou, Y. Zhang, Z. J. Wang, H. M. Weng, D. Prabhakaran, S.-K. Mo, Z. X. Shen, Z. Fang, X. Dai, Z. Hussain, and Y. L. Chen, Science **343**, 864 (2014).

[18] S. Borisenko, Q. Gibson, D. Evtushinsky, V. Zabolotnyy, B. Büchner, and R. J. Cava, Phys. Rev. Lett. **113**, 027603 (2014).

[19] Z. K. Liu, J. Jiang, B. Zhou, Z. J. Wang, Y. Zhang, H. M. Weng, D. Prabhakaran, S.-K. Mo, H. Peng, P. Dudin, T. Kim, M. Hoesch, Z. Fang, X. Dai, Z. X. Shen, D. L. Feng, Z. Hussain, and Y. L. Chen, Nat. Mater. **13**, 677 (2014).

[20] C.-X. Liu, S.-C. Zhang, and X.-L. Qi, Annu. Rev. Condens. Matter Phys. **7**, 301 (2016).

[21] R. Yu, W. Zhang, H.-J. Zhang, S.-C. Zhang, X. Dai, and Z. Fang, Science **329**, 61 (2010).

[22] Y. L. Chen, J.-H. Chu, J. G. Analytis, Z. K. Liu, K. Igarashi, H.-H. Kuo, X. L. Qi, S. K. Mo, R. G. Moore, D. H. Lu, M. Hashimoto, T. Sasagawa, S. C. Zhang, I. R. Fisher, Z. Hussain, and Z. X. Shen, Science **329**, 659 (2010).

[23] C.-Z. Chang, J. Zhang, M. Liu, Z. Zhang, X. Feng, K. Li, L.-L. Wang, X. Chen, X. Dai, Z. Fang, X.-L. Qi, S.-C. Zhang, Y. Wang, K. He, X.-C. Ma, and Q.-K. Xue, Adv. Mater. **25**, 1065 (2013).

[24] M. Li, C.-Z. Chang, L. Wu, J. Tao, W. Zhao, M. H. W. Chan, J. S. Moodera, J. Li, and Y. Zhu, Phys. Rev. Lett. **114**, 146802 (2015).

[25] Y. S. Hor, P. Roushan, H. Beidenkopf, J. Seo, D. Qu, J. G. Checkelsky, L. A. Wray, D. Hsieh, Y. Xia, S.-Y. Xu, D. Qian, M. Z. Hasan, N. P. Ong, A. Yazdani, and R. J. Cava, Phys. Rev. B **81**, 195203 (2010).

[26] C. Tang, C.-Z. Chang, G. Zhao, Y. Liu, Z. Jiang, C.-X. Liu, M. R. McCartney, D. J. Smith, T. Chen, J. S. Moodera, and J. Shi, Sci. Adv. **3**, e1700307 (2017).

[27] Z. Jiang, C.-Z. Chang, M. R. Masir, C. Tang, Y. Xu, J. S. Moodera, A. H. MacDonald, and J. Shi, Nat. Commun. **7**, 11458 (2016).

[28] W. Liu, L. He, Y. Xu, K. Murata, M. C. Onbasli, M. Lang, N. J. Maltby, S. Li, X. Wang, C. A. Ross, P. Bencok, G. van der Laan, R. Zhang, and K. L. Wang, Nano Lett. **15**, 764 (2015).

[29] Z. Jiang, C.-Z. Chang, C. Tang, P. Wei, J. S. Moodera, and J. Shi, Nano Lett. **15**, 5835 (2015).

[30] X. Che, K. Murata, L. Pan, Q. L. He, G. Yu, Q. Shao, G. Yin, P. Deng, Y. Fan, B. Ma, X. Liang, B. Zhang, X. Han, L. Bi, Q.-H. Yang, H. Zhang, and K. L. Wang, ACS Nano **12**, 5042 (2018).

[31] P. Li, J. Kally, S. S.-L. Zhang, T. Pillsbury, J. Ding, G. Csaba, J. Ding, J. S. Jiang, Y. Liu, R. Sinclair, C. Bi, A. DeMann, G. Rimal, W. Zhang, S. B. Field, J. Tang, W. Wang, O. G. Heinonen, V. Novosad, A. Hoffmann *et al.*, Sci. Adv. **5**, eaaw3415 (2019).

[32] W. Yang, S. Yang, Q. Zhang, Y. Xu, S. Shen, J. Liao, J. Teng, C. Nan, L. Gu, Y. Sun, K. Wu, and Y. Li, Appl. Phys. Lett. **105**, 092411 (2014).

[33] S. Zhu, D. Meng, G. Liang, G. Shi, P. Zhao, P. Cheng, Y. Li, X. Zhai, Y. Lu, L. Chen, and K. Wu, Nanoscale **10**, 10041 (2018).

[34] S. Zhu, G. Shi, P. Zhao, D. Meng, G. Liang, X. Zhai, Y. Lu, Y. Li, L. Chen, and K. Wu, Chin. Phys. B **27**, 076801 (2018).

[35] Q. L. He, X. Kou, A. J. Grutter, G. Yin, L. Pan, X. Che, Y. Liu, T. Nie, B. Zhang, S. M. Disseler, B. J. Kirby, W. Ratcliff II, Q. Shao, K. Murata, X. Zhu, G. Yu, Y. Fan, M. Montazeri, X. Han, J. A. Borchers, and K. L. Wang, Nat. Mater. **16**, 94 (2017).

[36] Q. L. He, G. Yin, L. Yu, A. J. Grutter, L. Pan, C.-Z. Chen, X. Che, G. Yu, B. Zhang, Q. Shao, A. L. Stern, B. Casas, J. Xia, X. Han, B. J. Kirby, R. K. Lake, K. T. Law, and K. L. Wang, Phys. Rev. Lett. **121**, 096802 (2018).

[37] J. S. Lee, A. Richardella, R. D. Fraleigh, C.-X. Liu, W. Zhao, and N. Samarth, npj Quantum Mater. **3**, 51 (2018).

[38] P. Wei, F. Katmis, B. A. Assaf, H. Steinberg, P. Jarillo-Herrero, D. Heiman, and J. S. Moodera, Phys. Rev. Lett. **110**, 186807 (2013).

[39] F. Katmis, V. Lauter, F. S. Nogueira, B. A. Assaf, M. E. Jamer, P. Wei, B. Satpati, J. W. Freeland, I. Eremin, D. Heiman, P. Jarillo-Herrero, and J. S. Moodera, Nature (London) **533**, 513 (2016).

[40] C. Lee, F. Katmis, P. Jarillo-Herrero, J. S. Moodera, and N. Gedik, Nat. Commun. **7**, 12014 (2016).

[41] C.-Y. Yang, L. Pan, A. J. Grutter, H. Wang, X. Che, Q. L. He, Y. Wu, D. A. Gilbert, P. Shafer, E. Arenholz, H. Wu, G. Yin, P. Deng, J. A. Borchers, W. Ratcliff, and K. L. Wang, Sci. Adv. **6**, eaaz8463 (2020).

[42] Q. L. He, G. Yin, A. J. Grutter, L. Pan, X. Che, G. Yu, D. A. Gilbert, S. M. Disseler, Y. Liu, P. Shafer, B. Zhang, Y. Wu, B. J. Kirby, E. Arenholz, R. K. Lake, X. Han, and K. L. Wang, Nat. Commun. **9**, 2767 (2018).

[43] F. Wang, D. Xiao, W. Yuan, J. Jiang, Y.-F. Zhao, L. Zhang, Y. Yao, W. Liu, Z. Zhang, C. Liu, J. Shi, W. Han, M. H. W. Chan, N. Samarth, and C.-Z. Chang, Nano Lett. **19**, 2945 (2019).

[44] L. Pan, A. Grutter, P. Zhang, X. Che, T. Nozaki, A. Stern, M. Street, B. Zhang, B. Casas, Q. L. He, E. S. Choi, S. M. Disseler, D. A. Gilbert, G. Yin, Q. Shao, P. Deng, Y. Wu, X. Liu, X. Kou, S. Masashi *et al.*, Adv. Mater. **32**, 2001460 (2020).

[45] L. D. Alegria, H. Ji, N. Yao, J. J. Clarke, R. J. Cava, and J. R. Petta, Appl. Phys. Lett. **105**, 053512 (2014).

[46] X. Yao, B. Gao, M.-G. Han, D. Jain, J. Moon, J. W. Kim, Y. Zhu, S.-W. Cheong, and S. Oh, Nano Lett. **19**, 4567 (2019).

[47] M. Mogi, T. Nakajima, V. Ukleev, A. Tsukazaki, R. Yoshimi, M. Kawamura, K. S. Takahashi, T. Hanashima, K. Kakurai, T.-h. Arima, M. Kawasaki, and Y. Tokura, Phys. Rev. Lett. **123**, 016804 (2019).

[48] R. Watanabe, R. Yoshimi, M. Kawamura, M. Mogi, A. Tsukazaki, X. Z. Yu, K. Nakajima, K. S. Takahashi, M. Kawasaki, and Y. Tokura, Appl. Phys. Lett. **115**, 102403 (2019).

[49] A. Kandala, A. Richardella, D. W. Rench, D. M. Zhang, T. C. Flanagan, and N. Samarth, Appl. Phys. Lett. **103**, 202409 (2013).

[50] M. M. Otrokov, I. I. Klimovskikh, H. Bentmann, D. Estyunin, A. Zeugner, Z. S. Aliev, S. Gaß, A. U. B. Wolter, A. V. Koroleva, A. M. Shikin, M. Blanco-Rey, M. Hoffmann, I. P. Rusinov, A. Y. Vyazovskaya, S. V. Eremeev, Y. M. Koroteev, V. M. Kuznetsov, F. Freyse, J. Sánchez-Barriga, I. R. Amiraslanov *et al.*, Nature (London) **576**, 416 (2019).

[51] Y. Gong, J. Guo, J. Li, K. Zhu, M. Liao, X. Liu, Q. Zhang, L. Gu, L. Tang, X. Feng, D. Zhang, W. Li, C. Song, L. Wang, P. Yu, X. Chen, Y. Wang, H. Yao, W. Duan, Y. Xu *et al.*, Chin. Phys. Lett. **36**, 076801 (2019).

[52] Y. Deng, Y. Yu, M. Z. Shi, Z. Guo, Z. Xu, J. Wang, X. H. Chen, and Y. Zhang, Science **367**, 895 (2020).

[53] M. Mogi, R. Yoshimi, A. Tsukazaki, K. Yasuda, Y. Kozuka, K. S. Takahashi, M. Kawasaki, and Y. Tokura, Appl. Phys. Lett. **107**, 182401 (2015).

[54] J. Ge, Y. Liu, J. Li, H. Li, T. Luo, Y. Wu, Y. Xu, and J. Wang, Natl. Sci. Rev. **7**, 1280 (2020).

[55] Y. Tokura, K. Yasuda, and A. Tsukazaki, Nat. Rev. Phys. **1**, 126 (2019).

[56] I. Lee, C. K. Kim, J. Lee, S. J. L. Billinge, R. Zhong, J. A. Schneeloch, T. Liu, T. Valla, J. M. Tranquada, G. Gu, and J. C. S. Davis, Proc. Natl. Acad. Sci. USA **112**, 1316 (2015).

[57] E. O. Lachman, A. F. Young, A. Richardella, J. Cuppens, H. R. Naren, Y. Anahory, A. Y. Meltzer, A. Kandala, S. Kempinger, Y. Myasoedov, M. E. Huber, N. Samarth, and E. Zeldov, Sci. Adv. **1**, e1500740 (2015).

[58] S. Qi, Z. Liu, M. Chang, R. Gao, Y. Han, and Z. Qiao, Phys. Rev. B **101**, 241407(R) (2020).

[59] Y. Jiang, Y. Y. Sun, M. Chen, Y. Wang, Z. Li, C. Song, K. He, L. Wang, X. Chen, Q.-K. Xue, X. Ma, and S. B. Zhang, Phys. Rev. Lett. **108**, 066809 (2012).

[60] P. Sessi, R. R. Biswas, T. Bathon, O. Storz, S. Wilfert, A. Barla, K. A. Kokh, O. E. Tereshchenko, K. Fauth, M. Bode, and A. V. Balatsky, Nat. Commun. **7**, 12027 (2016).

[61] W. Zhang, D. West, S. H. Lee, Y. Qiu, C.-Z. Chang, J. S. Moodera, Y. S. Hor, S. Zhang, and W. Wu, Phys. Rev. B **98**, 115165 (2018).

[62] Y. Ou, C. Liu, G. Jiang, Y. Feng, D. Zhao, W. Wu, X.-X. Wang, W. Li, C. Song, L.-L. Wang, W. Wang, W. Wu, Y. Wang, K. He, X.-C. Ma, and Q.-K. Xue, Adv. Mater. **30**, 1703062 (2018).

[63] Y. Yuan, X. Wang, H. Li, J. Li, Y. Ji, Z. Hao, Y. Wu, K. He, Y. Wang, Y. Xu, W. Duan, W. Li, and Q.-K. Xue, Nano Lett. **20**, 3271 (2020).

[64] Z. Huang, M.-H. Du, J. Yan, and W. Wu, Phys. Rev. Mater. **4**, 121202(R) (2020).

[65] H. Nakayama, M. Althammer, Y.-T. Chen, K. Uchida, Y. Kajiwara, D. Kikuchi, T. Ohtani, S. Geprägs, M. Opel, S. Takahashi, R. Gross, G. E. W. Bauer, S. T. B. Goennenwein, and E. Saitoh, Phys. Rev. Lett. **110**, 206601 (2013).

[66] Y.-T. Chen, S. Takahashi, H. Nakayama, M. Althammer, S. T. B. Goennenwein, E. Saitoh, and G. E. W. Bauer, Phys. Rev. B **87**, 144411 (2013).

[67] X. Zhou, L. Ma, Z. Shi, W. J. Fan, J.-G. Zheng, R. F. L. Evans, and S. M. Zhou, Phys. Rev. B **92**, 060402(R) (2015).

[68] Q. Shao, A. Grutter, Y. Liu, G. Yu, C.-Y. Yang, D. A. Gilbert, E. Arenholz, P. Shafer, X. Che, C. Tang, M. Aldosary, A. Navabi, Q. L. He, B. J. Kirby, J. Shi, and K. L. Wang, Phys. Rev. B **99**, 104401 (2019).

[69] Steven S.-L. Zhang and G. Vignale, Phys. Rev. Lett. **116**, 136601 (2016).

[70] M. Althammer, S. Meyer, H. Nakayama, M. Schreier, S. Altmannshofer, M. Weiler, H. Huebl, S. Geprägs, M. Opel, R. Gross, D. Meier, C. Klewe, T. Kuschel, J.-M. Schmalhorst, G. Reiss, L. Shen, A. Gupta, Y.-T. Chen, G. E. W. Bauer, E. Saitoh, and S. T. B. Goennenwein, Phys. Rev. B **87**, 224401 (2013).

[71] Y. Fan, P. Upadhyaya, X. Kou, M. Lang, S. Takei, Z. Wang, J. Tang, L. He, L.-T. Chang, M. Montazeri, G. Yu, W. Jiang, T. Nie, R. N. Schwartz, Y. Tserkovnyak, and K. L. Wang, Nat. Mater. **13**, 699 (2014).

[72] A. R. Mellnik, J. S. Lee, A. Richardella, J. L. Grab, P. J. Mintun, M. H. Fischer, A. Vaezi, A. Manchon, E.-A. Kim, N. Samarth, and D. C. Ralph, Nature (London) **511**, 449 (2014).

[73] J. Han, A. Richardella, S. A. Siddiqui, J. Finley, N. Samarth, and L. Liu, Phys. Rev. Lett. **119**, 077702 (2017).

[74] M. DC, R. Grassi, J.-Y. Chen, M. Jamali, D. Reifsnyder Hickey, D. Zhang, Z. Zhao, H. Li, P. Quarterman, Y. Lv, M. Li, A. Manchon, K. A. Mkhoyan, T. Low, and J.-P. Wang, Nat. Mater. **17**, 800 (2018).

[75] Y. Wang, P. Deorani, K. Banerjee, N. Koirala, M. Brahlek, S. Oh, and H. Yang, Phys. Rev. Lett. **114**, 257202 (2015).

[76] M. Jamali, J. S. Lee, J. S. Jeong, F. Mahfouzi, Y. Lv, Z. Zhao, B. K. Nikolić, K. A. Mkhoyan, N. Samarth, and J.-P. Wang, Nano Lett. **15**, 7126 (2015).

[77] H. Wu, Y. Xu, P. Deng, Q. Pan, S. A. Razavi, K. Wong, L. Huang, B. Dai, Q. Shao, G. Yu, X. Han, J.-C. Rojas-Sánchez, S. Mangin, and K. L. Wang, Adv. Mater. **31**, 1901681 (2019).

[78] N. H. D. Khang, Y. Ueda, and P. N. Hai, Nat. Mater. **17**, 808 (2018).

[79] M. Sawicki, W. Stefanowicz, and A. Ney, Semicond. Sci. Technol. **26**, 064006 (2011).

[80] M. Buchner, K. Höfler, B. Henne, V. Ney, and A. Ney, J. Appl. Phys. **124**, 161101 (2018).

[81] S. Foner, J. Appl. Phys. **79**, 4740 (1996).

[82] A. Moskaltsova, J. Krieft, D. Graulich, T. Matalla-Wagner, and T. Kuschel, AIP Adv. **10**, 015154 (2020).

[83] O. Inyang, L. Bouchenoire, B. Nicholson, M. Tokaç, R. M. Rowan-Robinson, C. J. Kinane, and A. T. Hindmarch, Phys. Rev. B **100**, 174418 (2019).

[84] P. Bougiatioti, O. Manos, O. Kuschel, J. Wollschläger, M. Tolkiehn, S. Francoual, and T. Kuschel, arXiv:1807.09032.

[85] C. Swindells, B. Nicholson, O. Inyang, Y. Choi, T. Hase, and D. Atkinson, Phys. Rev. Res. **2**, 033280 (2020).

[86] Z. Q. Qiu and S. D. Bader, Rev. Sci. Instrum. **71**, 1243 (2000).

[87] L. Ciorciaro, M. Kroner, K. Watanabe, T. Taniguchi, and A. Imamoglu, Phys. Rev. Lett. **124**, 197401 (2020).

[88] T. P. Lyons, D. Gillard, A. Molina-Sánchez, A. Misra, F. Withers, P. S. Keatley, A. Kozikov, T. Taniguchi, K. Watanabe, K. S. Novoselov, J. Fernández-Rossier, and A. I. Tartakovskii, Nat. Commun. **11**, 6021 (2020).

[89] M. Lang, M. Montazeri, M. C. Onbasli, X. Kou, Y. Fan, P. Upadhyaya, K. Yao, F. Liu, Y. Jiang, W. Jiang, K. L. Wong, G. Yu, J. Tang, T. Nie, L. He, R. N. Schwartz, Y. Wang, C. A. Ross, and K. L. Wang, Nano Lett. **14**, 3459 (2014).

[90] Y. Wu, G. Yin, L. Pan, A. J. Grutter, Q. Pan, A. Lee, D. A. Gilbert, J. A. Borchers, W. Ratcliff, A. Li, X.-d. Han, and K. L. Wang, Nature Elec. **3**, 604 (2020).

[91] G. Wu, D. Wu, Y. Ren, Q. Y. Jin, and Z. Zhang, Phys. Rev. B **103**, 014419 (2021).

[92] H.-T. He, G. Wang, T. Zhang, I.-K. Sou, G. K. L. Wong, J.-N. Wang, H.-Z. Lu, S.-Q. Shen, and F.-C. Zhang, Phys. Rev. Lett. **106**, 166805 (2011).

[93] Q. I. Yang, M. Dolev, L. Zhang, J. Zhao, A. D. Fried, E. Schemm, M. Liu, A. Palevski, A. F. Marshall, S. H. Risbud, and A. Kapitulnik, Phys. Rev. B **88**, 081407(R) (2013).

[94] V. M. Pereira, S. G. Altendorf, C. E. Liu, S. C. Liao, A. C. Komarek, M. Guo, H.-J. Lin, C. T. Chen, M. Hong, J. Kwo, L. H. Tjeng, and C. N. Wu, Phys. Rev. Mater. **4**, 064202 (2020).

[95] N. Nagaosa, J. Sinova, S. Onoda, A. H. MacDonald, and N. P. Ong, Rev. Mod. Phys. **82**, 1539 (2010).

[96] K. He, Y. Wang, and Q.-K. Xue, Natl. Sci. Rev. **1**, 38 (2013).

[97] J. Liu, A. Singh, Y. Y. F. Liu, A. Ionescu, B. Kuerbanjiang, C. H. W. Barnes, and T. Hesjedal, Nano Lett. **20**, 5315 (2020).

[98] F. Yang, A. A. Taskin, S. Sasaki, K. Segawa, Y. Ohno, K. Matsumoto, and Y. Ando, Appl. Phys. Lett. **104**, 161614 (2014).

[99] D.-X. Qu, Y. S. Hor, J. Xiong, R. J. Cava, and N. P. Ong, Science **329**, 821 (2010).

[100] N. Bansal, Y. S. Kim, M. Brahlek, E. Edrey, and S. Oh, Phys. Rev. Lett. **109**, 116804 (2012).

[101] C. Majkrzak, Phys. B: Condens. Matter **173**, 75 (1991).

[102] C. Majkrzak, Phys. B: Condens. Matter **213-214**, 904 (1995).

[103] J. Ankner and G. Felcher, J. Magn. Magn. Mater. **200**, 741 (1999).

[104] B. B. Maranville, B. J. Kirby, A. J. Grutter, P. A. Kienzle, C. F. Majkrzak, Y. Liu, and C. L. Dennis, J. Appl. Crystallogr. **49**, 1121 (2016).

[105] B. Kirby, P. Kienzle, B. Maranville, N. Berk, J. Krycka, F. Heinrich, and C. Majkrzak, Curr. Opin. Colloid Interface Sci. **17**, 44 (2012).

[106] H. D. Li, Z. Y. Wang, X. Kan, X. Guo, H. T. He, Z. Wang, J. N. Wang, T. L. Wong, N. Wang, and M. H. Xie, New J. Phys. **12**, 103038 (2010).

[107] S. E. Harrison, S. Li, Y. Huo, B. Zhou, Y. L. Chen, and J. S. Harris, Appl. Phys. Lett. **102**, 171906 (2013).

[108] P. A. Kienzle, Neutron activation and scattering calculator, https://www.ncnr.nist.gov/resources/activation.

[109] F. de Groot, Chem. Rev. **101**, 1779 (2001).

[110] J. Stöhr, J. Electron Spectrosc. Relat. Phenom. **75**, 253 (1995).

[111] J. Stöhr, H. A. Padmore, S. Anders, T. Stammler, and M. R. Scheinfein, Surf. Rev. Lett. **05**, 1297 (1998).

[112] J. E. Penner-Hahn, *X-Ray Absorption Spectroscopy* (Wiley Online Library, 2001).

[113] M. Abbate, J. Goedkoop, F. De Groot, M. Grioni, J. Fuggle, S. Hofmann, H. Petersen, and M. Sacchi, Surf. Interface Anal. **18**, 65 (1992).

[114] D. Vlachos, A. J. Craven, and D. W. McComb, J. Synchrotron Radiat. **12**, 224 (2005).

[115] S. Eisebitt, T. Böske, J.-E. Rubensson, and W. Eberhardt, Phys. Rev. B **47**, 14103 (1993).

[116] C. Piamonteze, Y. W. Windsor, S. R. V. Avula, E. Kirk, and U. Staub, J. Synchrotron Radiat. **27**, 1289 (2020).

[117] D. Yi, C. L. Flint, P. P. Balakrishnan, K. Mahalingam, B. Urwin, A. Vailionis, A. T. N'Diaye, P. Shafer, E. Arenholz, Y. Choi, K. H. Stone, J.-H. Chu, B. M. Howe, J. Liu, I. R. Fisher, and Y. Suzuki, Phys. Rev. Lett. **119**, 077201 (2017).

[118] A. Thompson, *X-Ray Data Booklet* (Lawrence Berkeley National Laboratory, University of California, 2001).

[119] M. Ye, W. Li, S. Zhu, Y. Takeda, Y. Saitoh, J. Wang, H. Pan, M. Nurmamat, K. Sumida, F. Ji, Z. Liu, H. Yang, Z. Liu, D. Shen, A. Kimura, S. Qiao, and X. Xie, Nat. Commun. **6**, 8913 (2015).

[120] S.-Y. Xu, M. Neupane, C. Liu, D. Zhang, A. Richardella, L. A. Wray, N. Alidoust, M. Leandersson, T. Balasubramanian, J. Sánchez-Barriga, O. Rader, G. Landolt, B. Slomski, J. H. Dil, J. Osterwalder, T.-R. Chang, H.-T. Jeng, H. Lin, A. Bansil, N. Samarth, and M. Z. Hasan, Nat. Phys. **8**, 616 (2012).

[121] L. B. Duffy, A. Frisk, D. M. Burn, N.-J. Steinke, J. Herrero-Martin, A. Ernst, G. van der Laan, and T. Hesjedal, Phys. Rev. Mater. **2**, 054201 (2018).

[122] A. I. Figueroa, F. Bonell, M. G. Cuxart, M. Valvidares, P. Gargiani, G. van der Laan, A. Mugarza, and S. O. Valenzuela, Phys. Rev. Lett. **125**, 226801 (2020).

[123] C.-C. Kao, C. T. Chen, E. D. Johnson, J. B. Hastings, H. J. Lin, G. H. Ho, G. Meigs, J.-M. Brot, S. L. Hulbert, Y. U. Idzerda, and C. Vettier, Phys. Rev. B **50**, 9599 (1994).

[124] D. R. Lee, S. K. Sinha, D. Haskel, Y. Choi, J. C. Lang, S. A. Stepanov, and G. Srajer, Phys. Rev. B **68**, 224409 (2003).

[125] S. Macke and E. Goering, J. Phys.: Condens. Matter **26**, 363201 (2014).

[126] F. Radu, A. Nefedov, J. Grabis, G. Nowak, A. Bergmann, and H. Zabel, J. Magn. Magn. Mater. **300**, 206 (2006).

[127] E. Benckiser, M. W. Haverkort, S. Brück, E. Goering, S. Macke, A. Frañó, X. Yang, O. K. Andersen, G. Cristiani, H.-U. Habermeier, A. V. Boris, I. Zegkinoglou, P. Wochner, H.-J. Kim, V. Hinkov, and B. Keimer, Nat. Mater. **10**, 189 (2011).

[128] R. F. Need, P. B. Marshall, E. Weschke, A. J. Grutter, D. A. Gilbert, E. Arenholz, P. Shafer, S. Stemmer, and S. D. Wilson, Phys. Rev. Mater. **2**, 093801 (2018).

[129] J. E. Hamann-Borrero, S. Macke, B. Gray, M. Kareev, E. Schierle, S. Partzsch, M. Zwiebler, U. Treske, A. Koitzsch, B. Büchner, J. W. Freeland, J. Chakhalian, and J. Geck, Sci. Rep. **7**, 13792 (2017).

[130] A. Bergmann, J. Grabis, A. Nefedov, K. Westerholt, and H. Zabel, J. Phys. D **39**, 842 (2006).

[131] M. Blume, J. Appl. Phys. **57**, 3615 (1985).

[132] S. Macke, A. Radi, J. E. Hamann-Borrero, A. Verna, M. Bluschke, S. Brück, E. Goering, R. Sutarto, F. He, G. Cristiani, M. Wu, E. Benckiser, H.-U. Habermeier, G. Logvenov, N. Gauquelin, G. A. Botton, A. P. Kajdos, S. Stemmer, G. A. Sawatzky, M. W. Haverkort *et al.*, Adv. Mater. **26**, 6554 (2014).

[133] J. Krieft, D. Graulich, A. Moskaltsova, L. Bouchenoire, S. Francoual, and T. Kuschel, J. Phys. D **53**, 375004 (2020).

[134] D. Graulich, J. Krieft, A. Moskaltsova, J. Demir, T. Peters, T. Pohlmann, F. Bertram, J. Wollschläger, J. R. L. Mardegan,

S. Francoual, and T. Kuschel, Appl. Phys. Lett. **118**, 012407 (2021).

[135] T. Kuschel, C. Klewe, J.-M. Schmalhorst, F. Bertram, O. Kuschel, T. Schemme, J. Wollschläger, S. Francoual, J. Strempfer, A. Gupta, M. Meinert, G. Götz, D. Meier, and G. Reiss, Phys. Rev. Lett. **115**, 097401 (2015).

[136] Q. Liu, C.-X. Liu, C. Xu, X.-L. Qi, and S.-C. Zhang, Phys. Rev. Lett. **102**, 156603 (2009).

[137] I. Vobornik, U. Manju, J. Fujii, F. Borgatti, P. Torelli, D. Krizmancic, Y. S. Hor, R. J. Cava, and G. Panaccione, Nano Lett. **11**, 4079 (2011).

[138] L. A. Wray, S.-Y. Xu, Y. Xia, D. Hsieh, A. V. Fedorov, Y. San Hor, R. J. Cava, A. Bansil, H. Lin, and M. Z. Hasan, Nat. Phys. **7**, 32 (2011).

[139] M. Li, C.-Z. Chang, B. J. Kirby, M. E. Jamer, W. Cui, L. Wu, P. Wei, Y. Zhu, D. Heiman, J. Li, and J. S. Moodera, Phys. Rev. Lett. **115**, 087201 (2015).

[140] M. Li, Q. Song, W. Zhao, J. A. Garlow, T.-H. Liu, L. Wu, Y. Zhu, J. S. Moodera, M. H. W. Chan, G. Chen, and C.-Z. Chang, Phys. Rev. B **96**, 201301(R) (2017).

[141] C. Klewe, T. Kuschel, J.-M. Schmalhorst, F. Bertram, O. Kuschel, J. Wollschläger, J. Strempfer, M. Meinert, and G. Reiss, Phys. Rev. B **93**, 214440 (2016).

[142] F. Wilhelm, P. Poulopoulos, A. Scherz, H. Wende, K. Baberschke, M. Angelakeris, N. K. Flevaris, J. Goulon, and A. Rogalev, Phys. Status Solidi (a) **196**, 33 (2003).

[143] F. Wilhelm, P. Poulopoulos, G. Ceballos, H. Wende, K. Baberschke, P. Srivastava, D. Benea, H. Ebert, M. Angelakeris, N. K. Flevaris, D. Niarchos, A. Rogalev, and N. B. Brookes, Phys. Rev. Lett. **85**, 413 (2000).

[144] P. Poulopoulos, F. Wilhelm, H. Wende, G. Ceballos, K. Baberschke, D. Benea, H. Ebert, M. Angelakeris, N. K. Flevaris, A. Rogalev, and N. B. Brookes, J. Appl. Phys. **89**, 3874 (2001).

[145] A. Mauger and C. Godart, Phys. Rep. **141**, 51 (1986).

[146] J. A. Krieger, Y. Ou, M. Caputo, A. Chikina, M. Döbeli, M.-A. Husanu, I. Keren, T. Prokscha, A. Suter, C.-Z. Chang, J. S. Moodera, V. N. Strocov, and Z. Salman, Phys. Rev. B **99**, 064423 (2019).

[147] A. Tcakaev, V. B. Zabolotnyy, C. I. Fornari, P. Rüßmann, T. R. F. Peixoto, F. Stier, M. Dettbarn, P. Kagerer, E. Weschke, E. Schierle, P. Bencok, P. H. O. Rappl, E. Abramof, H. Bentmann, E. Goering, F. Reinert, and V. Hinkov, Phys. Rev. B **102**, 184401 (2020).

[148] S.-W. Kim, H. Kim, J.-K. Kim, W.-S. Noh, J. Kim, K.-M. Kim, K.-S. Kim, J. S. Kim, J.-H. Park, and M.-H. Jung, APL Mater. **8**, 111108 (2020).

[149] B. Deng, Y. Zhang, S. B. Zhang, Y. Wang, K. He, and J. Zhu, Phys. Rev. B **94**, 054113 (2016).

[150] L. B. Duffy, N.-J. Steinke, D. M. Burn, A. Frisk, L. Lari, B. Kuerbanjiang, V. K. Lazarov, G. van der Laan, S. Langridge, and T. Hesjedal, Phys. Rev. B **100**, 054402 (2019).

[151] A. A. Serga, A. V. Chumak, and B. Hillebrands, J. Phys. D **43**, 264002 (2010).

[152] V. Cherepanov, I. Kolokolov, and V. L'vov, Phys. Rep. **229**, 81 (1993).

[153] S. Geller and M. A. Gilleo, Acta Crystallogr. **10**, 239 (1957).

[154] S. Geller, J. P. Remeika, R. C. Sherwood, H. J. Williams, and G. P. Espinosa, Phys. Rev. **137**, A1034 (1965).

[155] H. Chang, P. Li, W. Zhang, T. Liu, A. Hoffmann, L. Deng, and M. Wu, IEEE Magn. Lett. **5**, 6700104 (2014).

[156] B. Heinrich, C. Burrowes, E. Montoya, B. Kardasz, E. Girt, Y.-Y. Song, Y. Sun, and M. Wu, Phys. Rev. Lett. **107**, 066604 (2011).

[157] V. Castel, N. Vlietstra, B. J. van Wees, and J. B. Youssef, Phys. Rev. B **86**, 134419 (2012).

[158] S. M. Rezende, R. L. Rodríguez-Suárez, M. M. Soares, L. H. Vilela-Leão, D. Ley Domínguez, and A. Azevedo, Appl. Phys. Lett. **102**, 012402 (2013).

[159] Y. Fan, P. Quarterman, J. Finley, J. Han, P. Zhang, J. T. Hou, M. D. Stiles, A. J. Grutter, and L. Liu, Phys. Rev. Appl. **13**, 061002(R) (2020).

[160] Y. Sun, H. Chang, M. Kabatek, Y.-Y. Song, Z. Wang, M. Jantz, W. Schneider, M. Wu, E. Montoya, B. Kardasz, B. Heinrich, S. G. E. te Velthuis, H. Schultheiss, and A. Hoffmann, Phys. Rev. Lett. **111**, 106601 (2013).

[161] Y. M. Lu, Y. Choi, C. M. Ortega, X. M. Cheng, J. W. Cai, S. Y. Huang, L. Sun, and C. L. Chien, Phys. Rev. Lett. **110**, 147207 (2013).

[162] S. Geprägs, S. Meyer, S. Altmannshofer, M. Opel, F. Wilhelm, A. Rogalev, R. Gross, and S. T. B. Goennenwein, Appl. Phys. Lett. **101**, 262407 (2012).

[163] A. Quindeau, C. O. Avci, W. Liu, C. Sun, M. Mann, A. S. Tang, M. C. Onbasli, D. Bono, P. M. Voyles, Y. Xu, J. Robinson, G. S. D. Beach, and C. A. Ross, Adv. Elec. Mater. **3**, 1600376 (2017).

[164] V. H. Ortiz, M. Aldosary, J. Li, Y. Xu, M. I. Lohmann, P. Sellappan, Y. Kodera, J. E. Garay, and J. Shi, APL Mater. **6**, 121113 (2018).

[165] S. R. Yang, Y. T. Fanchiang, C. C. Chen, C. C. Tseng, Y. C. Liu, M. X. Guo, M. Hong, S. F. Lee, and J. Kwo, Phys. Rev. B **100**, 045138 (2019).

[166] H. Wang, J. Kally, J. S. Lee, T. Liu, H. Chang, D. R. Hickey, K. A. Mkhoyan, M. Wu, A. Richardella, and N. Samarth, Phys. Rev. Lett. **117**, 076601 (2016).

[167] Y. T. Fanchiang, K. H. M. Chen, C. C. Tseng, C. C. Chen, C. K. Cheng, S. R. Yang, C. N. Wu, S. F. Lee, M. Hong, and J. Kwo, Nat. Commun. **9**, 223 (2018).

[168] W. Liu, L. He, Y. Zhou, K. Murata, M. C. Onbasli, C. A. Ross, Y. Jiang, Y. Wang, Y. Xu, R. Zhang, and K. L. Wang, AIP Adv. **6**, 055813 (2016).

[169] T. Liu, J. Kally, T. Pillsbury, C. Liu, H. Chang, J. Ding, Y. Cheng, M. Hilse, R. Engel-Herbert, A. Richardella, N. Samarth, and M. Wu, Phys. Rev. Lett. **125**, 017204 (2020).

[170] C.-Y. Yang, Y.-H. Lee, K.-H. Ou Yang, K.-C. Chiu, C. Tang, Y. Liu, Y.-F. Zhao, C.-Z. Chang, F.-H. Chang, H.-J. Lin, J. Shi, and M.-T. Lin, Appl. Phys. Lett. **114**, 082403 (2019).

[171] P. Li, J. Ding, S. S.-L. Zhang, J. Kally, T. Pillsbury, O. G. Heinonen, G. Rimal, C. Bi, A. DeMann, S. B. Field, W. Wang, J. Tang, J. S. Jiang, A. Hoffmann, N. Samarth, and M. Wu, Nano Lett. **21**, 84 (2021).

[172] A. I. Snow, Phys. Rev. **85**, 365 (1952).

[173] W. J. Takei, D. E. Cox, and G. Shirane, Phys. Rev. **129**, 2008 (1963).

[174] Kunitomi, Nobuhiko, Hamaguchi, Yoshikazu, and Anzai, Shuichiro, J. Phys. France **25**, 568 (1964).

[175] W. Szuszkiewicz, B. Hennion, B. Witkowska, E. Ősuakowska, and A. Mycielski, Phys. Status Solidi (c) **2**, 1141 (2005).

[176] G. I. Makovetskii and G. M. Shakhlevich, Phys. Status Solidi (a) **61**, 315 (1980).

[177] L. M. Corliss, N. Elliott, J. M. Hastings, and R. L. Sass, Phys. Rev. **122**, 1402 (1961).

[178] P. Chen, Y. Zhang, Q. Yao, F. Tian, L. Li, Z. Qi, X. Liu, L. Liao, C. Song, J. Wang, J. Xia, G. Li, D. M. Burn, G. van der Laan, T. Hesjedal, S. Zhang, and X. Kou, Nano Lett. **20**, 1731 (2020).

[179] D. N. Astrov, J. Exptl. Theoret. Phys. (U.S.S.R.) **40**, 1035 (1961).

[180] S. V. Eremeev, V. N. Men'shov, V. V. Tugushev, P. M. Echenique, and E. V. Chulkov, Phys. Rev. B **88**, 144430 (2013).

[181] M. M. Otrokov, T. V. Menshchikova, M. G. Vergniory, I. P. Rusinov, A. Y. Vyazovskaya, Y. M. Koroteev, G. Bihlmayer, A. Ernst, P. M. Echenique, A. Arnau, and E. V. Chulkov, 2D Mater. **4**, 025082 (2017).

[182] C. Ophus, Microsc. Microanal. **25**, 563 (2019).

[183] A. Edström, A. Lubk, and J. Rusz, Phys. Rev. B **99**, 174428 (2019).

[184] N. Shibata, S. D. Findlay, Y. Kohno, H. Sawada, Y. Kondo, and Y. Ikuhara, Nat. Phys. **8**, 611 (2012).

[185] J. Chapman, P. Batson, E. Waddell, and R. Ferrier, Ultramicroscopy **3**, 203 (1978).

[186] P. Schattschneider, S. Rubino, C. Hébert, J. Rusz, J. Kuneš, P. Novák, E. Carlino, M. Fabrizioli, G. Panaccione, and G. Rossi, Nature (London) **441**, 486 (2006).

[187] J. G. Checkelsky, J. Ye, Y. Onose, Y. Iwasa, and Y. Tokura, Nat. Phys. **8**, 729 (2012).

[188] D. A. Abanin and D. A. Pesin, Phys. Rev. Lett. **106**, 136802 (2011).

[189] T. Dietl, H. Ohno, and F. Matsukura, Phys. Rev. B **63**, 195205 (2001).

[190] J.-J. Zhu, D.-X. Yao, S.-C. Zhang, and K. Chang, Phys. Rev. Lett. **106**, 097201 (2011).